



HAL
open science

Pore structure and interdisciplinary analyses in Roman mortars: Building techniques and durability factors identification

Paloma Pineda, Santiago Medina-Carrasco, Alfredo Iranzo, Laetitia Borau,
Iván García-Jiménez

► To cite this version:

Paloma Pineda, Santiago Medina-Carrasco, Alfredo Iranzo, Laetitia Borau, Iván García-Jiménez. Pore structure and interdisciplinary analyses in Roman mortars: Building techniques and durability factors identification. *Construction and Building Materials*, 2021, 317, <https://www.sciencedirect.com/science/article/pii/S0950061821035546>. 10.1016/j.conbuildmat.2021.125821 . hal-03485144

HAL Id: hal-03485144

<https://hal.science/hal-03485144>

Submitted on 29 Jan 2024

HAL is a multi-disciplinary open access archive for the deposit and dissemination of scientific research documents, whether they are published or not. The documents may come from teaching and research institutions in France or abroad, or from public or private research centers.

L'archive ouverte pluridisciplinaire **HAL**, est destinée au dépôt et à la diffusion de documents scientifiques de niveau recherche, publiés ou non, émanant des établissements d'enseignement et de recherche français ou étrangers, des laboratoires publics ou privés.



Contents lists available at ScienceDirect

Construction and Building Materials

journal homepage: www.elsevier.com/locate/conbuildmat

Pore structure and interdisciplinary analyses in Roman mortars: Building techniques and durability factors identification

Paloma Pineda^{a,*}, Santiago Medina-Carrasco^b, Alfredo Iranzo^c, Laetitia Borau^d, Iván García-Jiménez^e

^a Department of Building Structures and Geotechnical Engineering, School of Architecture, Universidad de Sevilla, Avda. Reina Mercedes, No. 2, 41012 Sevilla, Spain

^b X-Ray Laboratory (CITUS), Universidad de Sevilla, Avda. Reina Mercedes, 4B, 41012 Sevilla, Spain

^c Thermal Engineering Group, Energy Engineering Department, School of Engineering, Universidad de Sevilla, Camino de los Descubrimientos s/n, 41092 Sevilla, Spain

^d CNRS, Ausonius, Bordeaux, France

^e Conjunto Arqueológico de Baelo Claudia, Agencia Andaluza de Instituciones Culturales, Ensenada de Bolonia s/n, 11380 Tarifa, Cádiz, Spain

ARTICLE INFO

Keywords:

Hydraulic structures
Roman mortar
Durable materials
Pore structure
Heritage preservation
Computed Tomography
Multidisciplinary analyses

ABSTRACT

Microstructural and compositional analysis of historical mortars is an active research field, not only to guarantee the use of compatible repair measures, but also to guide the design of novel efficient materials. Despite the crucial role of Roman mortars in building history, there is a significant lack of knowledge of their pore system in relation to building techniques and durability. From these premises, this research focuses on the structural mortars of the Realillo aqueduct (Archaeological Site of Baelo Claudia, Spain). This construction is especially interesting from a durability point of view, as in addition to being in a windy coastal area, the water-proof potential of the material is a major issue. Complementary experimental techniques (petrography, computed tomography, X-ray fluorescence, X-ray diffraction (micro and conventional), thermal analysis, pycnometry, physisorption, Hg porosimetry, and SEM-EDS) are applied within a multidisciplinary approach, including the Vitruvian guidelines and comparative analysis with coetaneous buildings. The size and shape of the pores and the porous volume distribution have been linked to hydraulicity, and to cohesion and weathering resistance. Total and open porosity can be related to waterproof worsening, and the entrapped air pores detected could indicate inadequate placement. The shrinkage cracks can be related to the sea sand aggregate. Thermal analysis and C-A-S-H gel indicate hydraulic phases, but with different hydraulicity levels. This variation could be related to the non-high-purity limestone and/or to the recipe. The differences in binder/aggregate ratios and petrographic classification confirm the distinct compositions. Non-standardized manufacturing or building stages could be related to compositional variations. This research has provided significant insights into durability and manufacturing issues by integrating a micro-macro pore structure study within multianalytical and interdisciplinary research. The method may be used as a complementary procedure to characterize historical mortars. As upgrading/degrading durability factors were obtained, a conservation campaign could be designed. In addition, knowledge about historical building techniques and materials has been enriched.

1. Introduction

In heritage structures, the nature of building materials, and especially mortars, plays a major role in ensuring and enhancing durability. Durability is linked to the capability of a building material to resist different damage mechanisms. Moreover, the static and dynamic structural behaviour is strongly related to the mechanical, chemical, and microstructural properties of mortars [1]. Microstructural characteristics provide a relevant guide not only for selecting possible repair

mortars [2], but also to enrich the knowledge about historical building techniques, as well as the heritage value of structural materials. Furthermore, the design of novel, durable, and eco-efficient materials can be inspired by the properties of ancient mortars [3]. One of the most critical properties of mortars from historical constructions is porosity and its relationship to moisture content and water transport mechanisms, as both play a relevant role in the degeneration phenomenon. In addition to having a direct impact on moisture transport, mechanical performance, durability, and compatibility of building materials, the

* Corresponding author.

E-mail address: palomapineda@us.es (P. Pineda).

<https://doi.org/10.1016/j.conbuildmat.2021.125821>

Received 29 July 2021; Received in revised form 10 November 2021; Accepted 23 November 2021

Available online 8 December 2021

0950-0618/© 2021 The Author(s).

Published by Elsevier Ltd.

This is an open access article under the CC BY-NC-ND license

(<http://creativecommons.org/licenses/by-nc-nd/4.0/>).

pore structure can provide relevant information on how heritage building materials were manufactured. The microstructure (in terms of porosity, pore size, and distribution) is related to the carbonation rate and to the dimensions of the calcite crystal and aggregates [4], and therefore has an impact on hardening. The composition and size of the raw materials (especially aggregates and binder) also have an impact on the microstructure.

In the waterproof mortars of historic buildings (e.g., baths, cisterns, etc.), it was common to use slaked lime and pozzolanic materials in the binder matrix and crushed bricks of different sizes for aggregates [5]. The use of lime binders dates to the 6th millennium BC and, although most ancient mortars in Europe are lime-based, those manufactured by the Romans stand out by their quality and durability [6,7]. Thus, the Romans were masters of using mortar as a control factor of cracking phenomena, minimizing local collapse by adding the right amount of elastic materials [6,7]. The addition of brick fragments within the lime matrix, a common practice during that period, affects both hydraulic reactivity and physical–mechanical behaviour (i.e., porosity, transpirability, lightness, and adhesion) [8]. One of the most relevant differences between Roman mortars and modern mortars is the porosity and pore structure (especially the fluid pathways within the matrix). The relation between small pore size and high porosity is directly related to the satisfactory durability of Roman mortars [9]. The singular pore structure of Roman mortars can be attributed to the vesicular structure of pozzolanic materials [10]. In these mortars, hydrated lime together with natural pozzolan or brick dust generates a high hydraulic continuous microcrystalline matrix [5], and the properties of the lime produce a high microporosity level that enhances the carbonation degree [11]. The mortar compressive strength depends on porosity and hydraulicity [12] and is also related to the carbonation process, since, in lime mortars, progressive carbonation increases the strength and decreases porosity [13]. The morphology of the porous structure provides a clear space for the secondary crystallization of calcite [5]. Thus, some mineral phases settle in the pores of pozzolanic materials (e.g., C-A-S-H). This chemical process, which occurs without cracking, provides an improvement in compactness. The porous structure formed delays fluid diffusion within the matrix [14], increasing strength, ductility, and water resistance [10,15]. As mentioned above, porosity is also related to the manufacturing technique. Therefore, under high burning temperatures and long calcination periods, both shrinkage and density are high, and porosity and chemical reactivity are low [16]. If during manufacturing both the burning temperature and the duration are low, a soft-burned mortar is obtained, the material has a lower density and shrinkage, and the porosity and chemical reactivity are higher [16]. Furthermore, the more water is added to the mix, the higher porosity obtained [11].

A comprehensive analysis of the pore system is required for a reliable characterization of historical structural mortars, but taking into account that, as stated by Thomson et al. [13], different techniques can provide different values for the same sample, being essential the interpretation of the results, as well as its influence on the entire material behaviour.

From the aforementioned, it is clear that, if the microstructure and composition of the material are thoroughly analysed, it is possible not only to detect weaknesses or select compatible repair materials but also to enrich the knowledge about different heritage features, such as historical building techniques. In that sense, different experimental techniques can provide relevant data on pore system morphology and physical–chemical properties. Computed tomography (CT) images and microphotographs allow for analysing the microstructure from a qualitative point of view. Petrographic images can provide information on the mineralogical and chemical composition, as well as manufacturing features, such as the binder-aggregate ratio. Scanning electron microscopy (SEM) together with energy dispersive spectroscopy (EDS) is frequently used to obtain both morphological and compositional data, including the feasibility of detecting calcium silicate hydrate (C-S-H) and calcium aluminium silicate hydrate (C-A-S-H) [14,17,18]. Those gel

phases improve durability, increasing resistance to environmental damage [3]. Mercury intrusion porosimetry (MIP) can provide relevant data on the microstructural characteristics of the mortar (pore size distribution) within the mesopore and macropore ranges. In the micropore and mesopore ranges, physisorption is a valuable technique for use. X-ray fluorescence (XRF) and X-ray diffraction (XRD) are also especially useful in the characterization of heritage materials. XRF is a widely used technique to determine the elemental characterization of heritage materials [19]. By using this type of analysis, the samples can be examined with minimal preparation, and minimal or no pre-treatment is necessary in most cases. This technique allows for obtaining the results in a fast way -only a few minutes are required- being an effective and advantageous procedure from a cost point of view [11,19,20]. To characterize the crystalline phases of archaeological samples, XRD is a commonly used technique with multiple applications [20–22]. Micro X-ray diffraction (μ -XRD) is a variant of XRD that provides a detailed analysis of solid sample areas, and neither material transformation nor grinding are required. This non-destructive character has multiple advantages, especially in archaeometry studies [23,24]. The use of 2D detectors provides additional information on the size and shape of the crystallites. The reason for this is that, by studying the rings, it is possible to obtain very fast results with a resolution higher than that of the 0D or 1D detectors [25,26]. Thermal analyses, such as thermogravimetric analysis (TGA) and differential scanning calorimetry (DSC), are also widely recognized as useful procedures to be used in the characterization of heritage building mortars, providing a good understanding of their thermal behaviour, and showing different temperature regions where decomposition processes are occurring [6,7]. These analyses also provide information on the manufacturing process, on crystalline transitions (exo or endothermic) and on the main components, including the aggregate type [8,27]. Thermal transformations such as dehydration, dehydroxylation, oxidation, and decomposition can be determined, and the reactions associated with controlled heating of the mortar can be evaluated [28]. Those procedures are especially useful if the main concern is to determine the hydraulic nature [29]. In addition, thermal analyses are useful in the selection of repair materials, as they must be compatible with the substrate in terms of reverse hydraulicity index and CO₂ loss [2].

It should be noted that although porosity characterization is well established for cement-based materials, few studies focus on lime-based materials [30]. As far as Roman mortars are concerned, it can be said that the lack of knowledge on that issue is significant. In addition, the evaluation should be performed using a multidisciplinary methodology that links materials science, archaeology, geology, and architecture. As Roman mortars are paradigmatic materials within the building history, more research is required from updated approaches.

In this research, representative structural mortars from the Realillo aqueduct, a water-related construction of the Archaeological Site of Baelo Claudia, are analysed (Fig. 1). The mortars were obtained from the water supply (aqueduct, drop shaft, and settling tank) and storage structures (water tower) dated to the early Roman Empire (probably the 1st century CE and at least used until the 3rd century CE) which were recently excavated (General Research Project directed by Laetitia Borau (CNRS, France): Water management and construction techniques in the territory of Baelo Claudia during the Antiquity) [31–33]. The archaeological site of the ancient Spanish-Roman city of Baelo Claudia is located at the southernmost point of the Iberian Peninsula, in the Bolonia cove, in the Strait of Gibraltar. This is a highly strategic place that conditioned the location and construction of the city in ancient times. Being an uninterrupted inhabited city since the 2nd century BCE to the 7th century CE, it achieved the rank of Municipio during the 1st century CE. The city became a commercial emporium, which was characterized by its proximity to Africa, and by its large and well-developed salting “industry” that was founded on the richness of the Strait waters. Archaeological excavations carried out since the beginning of the twentieth century have brought to light the best preserved monumental complex from the

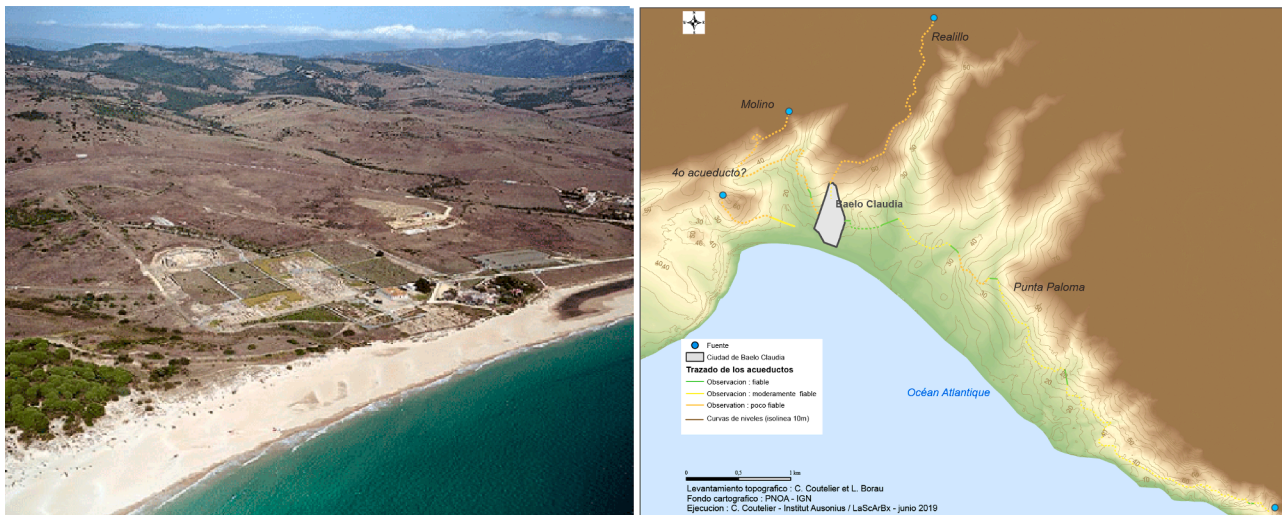


Fig. 1. General view of Baelo Claudia (left) and the location of the Realillo aqueduct (right).

High Imperial period in the Iberian Peninsula, a true paradigm of Roman urbanism [34]. As a singular fact, it is possible to identify most of the characteristic elements of an ancient city. The monumental area (forensic zone and temples), together with a theatre, several thermal complexes, a wall layout (with at least 25 towers and three monumental gates), three aqueducts, and an orthogonal urban layout (perfectly identified) shape this exceptional site. In addition, a large salting factory area located south of the city can be partially identified.

The goal of this work is to provide microstructural and compositional characterization of the selected materials, with a special focus on building techniques and durability features. Furthermore, since the

ensemble is located in a coastal area, the potential of environmental conditions as damage factors should be considered [35]. The microstructure and physical–chemical properties are studied in terms of the pore system, morphology, composition, density, and surface area using different experimental techniques. In particular, significant insights regarding material durability and manufacturing techniques are obtained from a combined analysis of Computed Tomography together with microstructure investigation, covering from the micropore to macropore range. This, together with the interdisciplinary approach, is one of the main novelties of this work and may be established as a complementary method for characterizing historical mortars. In



Fig. 2. Location of the samples: (a) Bearing wall of the channel; (b) wall of the drop shaft of the aqueduct; (c) Inside view of the drop shaft; (d) south wall of the settling tank; (e) channel of the Realillo aqueduct feeding the water tower; (f) east wall of the water tower; (g) west wall of the water tower.

addition, to provide an adequate contextualization, a comparison among the main properties of the analysed materials and Roman mortars from water-related and/or coetaneous buildings analysed in recent research works (last 10 years) is presented and discussed. The results from this work will allow for: (i) enhancing the knowledge on the building techniques from a heritage framework, (ii) increasing the knowledge of the upgrading/degrading durability mechanisms of Roman mortars located in aggressive environments (sea-water attack, high humidity content, and sand erosion), and (iii) selecting compatible repair materials for future retrofitting-strengthening-refurbishment works.

2. Materials and methods

2.1. Materials

Mortar samples were obtained following the method proposed by Binda et al. [36] under the supervision of the authority in charge. Detached or semi-detached fragments were removed from the main structural parts (Fig. 2).

The mortars have been classified into five different groups, depending on their use as building materials: (i) Group A, structural mortar of the masonry bearing wall of the channel, (ii) Group B, structural mortars of the drop shafts, (iii) Group C, structural mortar of the settling tank, (iv) Group D, mortar of the channel of the aqueduct, and (v) Group E, structural mortars of the water tower.

2.2. Methods

The experimental campaign has been designed as depicted in Fig. 3. A complete description of the experimental methods is provided in the following paragraphs.

In the first stage, the main objective was to obtain general chemical data, with a special focus on the hydraulic nature of the whole mortar (stage 01 in the flow diagram, Fig. 3). To achieve this, XRF, μ -XRD, and DSC-TGA analyses were performed. From this preliminary step, the higher hydraulicity level mortars are identified. The highest hydraulicity material is then selected and analysed by conventional XRD (stage 01b, Fig. 3). After grinding in agate mortar, both the whole mortar

(sieved fraction less than 100 μm) and the binder (fraction less than 63 μm) are studied. Phase identification is carried out using the Rietveld method. A detailed description of the procedures and devices is provided in the following paragraphs.

- **XRF.** A sequential wavelength dispersive X-ray fluorescence spectrometer, AXIOS model (PANalytical, the Netherlands) with a 4 kW Rh tube was used. This equipment allows for quantitative chemical analysis in a wide range of concentrations, from major components to traces. By grinding in agate mortar, the powder was obtained from small pieces of the samples and dried at 105° C. The fused beads were prepared for major analysis, containing 0.8 g of pulverized sample mixture with 7.2 g of lithium metaborate-tetraborate (34–66 %wt) acting as flux. Loss of ignition (L.O.I.) was calculated after calcination of 1 g of sample at 1000 °C for 2 h.
- **μ -XRD.** The equipment used was a D8 DISCOVER diffractometer equipped with a 2D detector model VANTEC-500 (Bruker, Germany) with a copper K α radiation source (0.15405 nm wavelength); A 1 mm capillary was used, obtaining three 2D frames for each point from 20° to 60° 2 θ , with a step width of 20° and a time per step of 60 s, with tube conditions of 40 kV and 40 mA. Each frame covered approximately 30° 2 θ . A video laser system allowed the adjustment and position of the samples and analysis areas. The PDF-4 + 2020 database (International Centre for Diffraction Data (ICDD)) implemented in the Bruker DIFFRAC.EVA 5.2 software was used to identify the crystalline phases. A semi-quantification using the RIR method [40,41] allows for obtaining the phase wt %.
- **XRD.** Conventional X-ray diffraction (XRD) was performed using a D8 ADVANCE powder diffractometer, equipped with a high resolution VANTEC-1 position sensitive detector (Bruker, Germany), and complemented by a radial Soller slit system with a copper K α radiation source (0.15405 nm wavelength). XRD scans were performed in a 10°- 70° 2 θ range (0.02° step and 0.2 s step time). The characteristics of the X-ray tube were 40 kV and 40 mA. The powder diffractometer was calibrated according to the manufacturer's specifications. Corundum, LaB6 and silicon standards were tested in a wide range of 2 θ angles to verify the resolution and compute the instrumental contribution for structural adjustments. Bruker Topas 6 software was used to fit the recorded diffractograms [42]. The

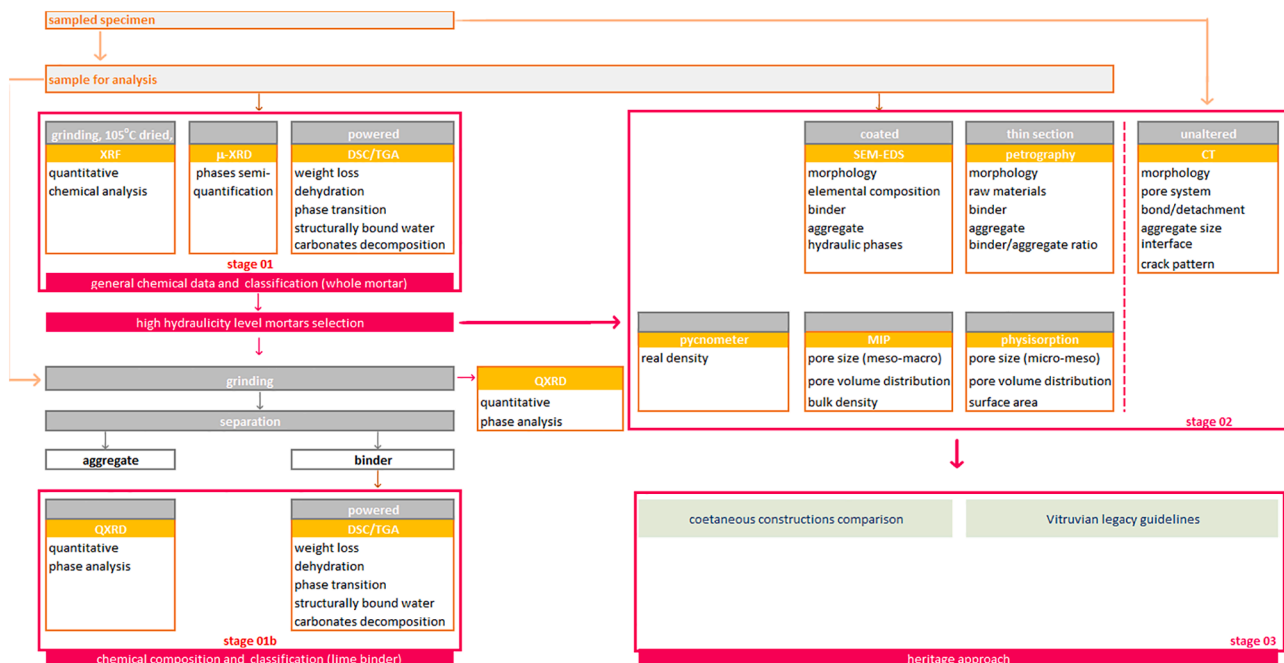


Fig. 3. Method flow chart based on RILEM recommendations [37–39].

relative content of the phases (in wt%) was obtained using the Rietveld method [43,44]. Crystalline phases were identified by applying the PDF-4 + 2020 database (International Centre for Diffraction Data (ICDD)) with Bruker DIFFRAC.EVA 5.2 software. To achieve the best fit, the fundamental parameters method was applied with a detailed description of the diffractometer [42]. Zero error (2θ) as well as absorption and lattice parameters were treated as adjustable parameters. Lorentz polarization geometric factors were used according to the configuration. Background adjustment was made in fourth order.

- **DSC-TGA.** In thermal analysis, both the weight change (TGA) and differential heat flow (DSC) were measured. Thermogravimetric measurements (DSC/TGA) were performed with a SDT Q600 thermobalance, with a temperature gradient of 10 °C/min up to 1000 °C in an atmosphere of N₂ (100 mL/min). The balance sensitivity was 0.1 µg, and the calorimetric precision was ± 2%. Heat flow integrations were automatically normalized using the dynamic weight at the start of each transition.

In the second stage (02 in Fig. 3), the microstructure and physical properties analysis (pore system, morphology, density, and surface area) was carried out in the samples that exhibit the highest hydraulic potential. The analytical procedures are MIP, physisorption (Phy), helium pycnometry (Pyc), X-ray CT, petrographic analysis, and SEM-EDS.

- **MIP.** The pore system within the meso-macropore range was analysed by means of the mercury intrusion porosimetry (MIP) technique, using an automated mercury porosimeter Poremaster 60GT (Quantachrome Instruments). Measuring the Hg volume that was intruded into the samples as a function of increasing pressure, it was possible to determine the pore size and the pore volume distribution. The pressure range was 0.2–60,000 psia, the pore size range was 1100–0.0036 µm, the volume precision was ±1% fso of the volume of the sample cell stem, and the volume resolution was ± 0.0001 cm³.
- **Physisorption.** A physisorption device (ASAP 2420 micromeritics) was also used to obtain surface area and complementary pore data within the micro and mesopore range (volume and size).
- **Helium pycnometry.** The real density was determined using a helium pycnometer (Pentapycnometer 5200E, Quantachrome) with a pressure range of 1–20 psig and a resolution of 0.0001 g/cm³. The bulk density was calculated from porosimeter analysis as follows: bulk density = sample mass/(sample apparent volume), where the apparent volume was determined as (mass/real density + intruded volume).
- **X-ray CT.** X-ray computed tomography equipment (Y.Cougar SMT, YXLON) was used to analyse the microstructure from a qualitative point of view. The equipment has an open microfocus tube (multi-focus optional, MFT) with tungsten as the target material, and the detail detectability is less than 1 mm (<350 nm with MFT). The maximum geometric magnification is 2,000x, and the total magnification is 17,500x.
- **Petrographic analysis.** A Nikon LV100ND POL/DS polarizing/dispersion microscope was used to obtain microphotographs of representative fragments. In the preparation of thin sections, to maintain the samples as unaltered as possible, they were preconsolidated by means of resin impregnation under vacuum. The sections were then cut and polished to a standard thickness of 30 µm.
- **SEM-EDS.** Micrographs and elemental composition were obtained with a FEI Teneo field emission scanning electron microscope (SEM) combined with energy-dispersive X-ray spectroscopy (EDS). The AITM-0004 protocol and these key specifications were applied: voltage 5 kV, angle 90°, ETD, and EDS detectors for semiquantitative analysis and mapping, different magnifications related to Polaroid 5', 125 × 95 mm image size. A platinum sputtered coating (10 nm thickness) was applied to the samples using a Leica AC600 sputter coater.

The procedure is completed with the heritage framework, by providing a comparative analysis with coetaneous constructions, and with the Vitruvian guidelines (stage 03 in Fig. 3).

It is worth highlighting that, in all stages, the analysis of properties that are related to durability and manufacturing techniques is a main issue. Fig. 4 provides a description of the mortars and the tests that have been performed.

The tests were carried out with the support and equipment of "Servicios Generales de Investigación- Universidad de Sevilla" in these departments: Functional Characterization, Microscopy, and X-ray Lab.

3. Results and discussion

3.1. Compositional characterization and thermal analysis

X-ray fluorescence has provided the chemical composition in terms of the major oxides (in wt%) (Table 1). High amounts of Si and Ca are the main components, and small amounts of Al, Fe, and Mg are also detected. From the high amount of Ca, it can be concluded that the materials are lime mortars, and the presence of Si could be attributed to the use of quartz sand in the mix [28,45]. An exception are samples 06 and 07 with a higher concentration of Fe, which, as later observed by diffraction, should appear in an amorphous form. The high Mn content of sample 06 is also an exception. The high Fe and Mn content could be attributed to the aggregates. Furthermore, it can be related to the mineral profile of the area (high montmorillonite and iron oxide content, as well as pyrolusite [46,47]).

The micro-XRD results show that the samples are basically composed of calcite and quartz, with a much higher proportion, in general, of calcite. A semiquantification of the phase through the RIR method [40,41] provides calcite and quartz (wt %). The µ-XRD results are consistent with those of XRF. Thus, it can be concluded that recarbonated lime is detected in the materials. The observed recarbonated lime is characterized by a microcrystalline structure and could also be related to the thermal decomposition of carbonates from ceramic materials [28,45]. The use of quartz sand and lime as raw materials can also be asserted from these experimental results. In general, for the samples, inhomogeneous rings are observed in the µ-XRD 2D frames [25,26], as a result of large quartz crystallites. Texture is observed in many of the samples, with peaks of much greater intensity in the diffractogram than those of the pattern. This texturing phenomenon is normal in natural samples where grinding has not been carried out for the XRD study [48]. In the XRD images (Fig. 5), the peaks of the 2θ diffractogram obtained from the integration of the 2D frames match the rings of the frames. The laser-marked analysis areas are highlighted. Table 2 summarizes the µ-XRD results, where the calcite, magnesium calcite, and quartz phases correspond to the standards PDF 04-012-0489, PDF 01-089-1304 and PDF 00-005-0490 from the PDF-4 + 2020 database (International Centre for Diffraction Data (ICDD)).

Fig. 6 shows the diffractograms of sample 05 for the whole mortar (sieved < 100 µm) and the binder fraction (<63 µm). The main Bragg peaks of the detected phases are marked. Quartz phases (PDF 04-012-0489) and magnesium calcite (PDF 01-089-1304) phases are detected, as well as montmorillonite (PDF 01-0003-014) and aragonite (PDF 01-041-1475) in smaller quantities. It is remarkable how the sieving clearly reduces the intensity and therefore the amount of quartz. This could be simply explained from a physical point of view, as there is greater difficulty for the hardest material (quartz) to be ground with the sieve size. Qualitatively, Fig. 6 clearly shows a decrease in the quartz content that would confirm that the aggregates were mainly quartzitic.

Phase percentages were also quantified in sample 05 (whole mortar and binder) by Rietveld adjustment (Table 3). The goodness-of-fit (GOF) and weighted profile R factor (R_{wp}), as well as the R_{Bragg} obtained for the different phases are also shown. Adequate values have been obtained for adjustment [42,44]. A decrease in quartz (29.1–13.5 wt%) and a decrease in aragonite (8.5–3.4 wt%) are observed depending on the





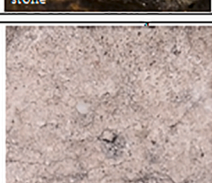
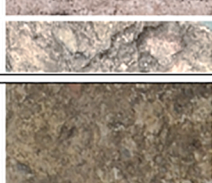
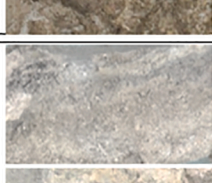

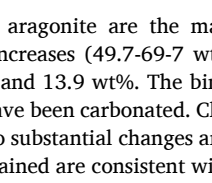
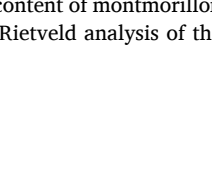
Group	Image	Code	Type and location	Experimental technique																	
				XRF	μ-XRD	XRD	DSC/TGA	Pyc	P	CT	MIP	Phy	SEM-EDS								
Group A		01	structural mortar of the masonry bearing wall of the channel (North area)																		
		02	structural mortar of the masonry bearing wall of the channel (North area)	X	X			X	X			X									
		08	structural mortar of the masonry bearing wall of the channel (room No1)	X	X																
Group B		03	structural mortar of the dropshaft (No1) that is connected to the bearing wall of the channel	X	X			X	X	X	X	X	X	X	X	X	X	X	X	X	X
		04	structural mortar of the dropshaft (No2)	X	X			X	X			X	X	X	X	X	X	X	X	X	X
Group C		05	structural mortar of the settling tank	X	X	X		X	X	X	X	X	X	X	X	X	X	X	X	X	X
		06	structural mortar of the settling tank	X	X			X	X			X									
Group D		07	mortar of the channel of the aqueduct	X	X			X	X	X											
Group E		09	structural mortar of the water tower (North wall)	X	X			X	X												
		10	structural mortar of the water tower (East wall)	X	X			X	X	X											

Fig. 4. Mortar samples: group, image, code, type, location, and applied techniques.

sieving. Quartz and aragonite are the main aggregate components. Magnesium calcite increases (49.7-69.7 wt%) and the clay phase remains between 12.7 and 13.9 wt%. The binder is mainly composed of CaO, which would have been carbonated. Clay could be associated with the aggregate, and no substantial changes are observed in the two sieve sizes. The phases obtained are consistent with the mineralogical profile of the location (rich content of montmorillonite and aragonite [46,47]).

Fig. 7 shows the Rietveld analysis of the XRD pattern obtained for

sample 05, depicting the experimental diffractogram (blue line) and the Rietveld best fit (red). The bottom grey line shows the deviation between the best fit and experimental diffractograms. The whole mortar composition is: 29.1 wt% quartz, 49.7 wt% magnesium calcite, 12.7 wt% montmorillonite, and 8.5 wt% aragonite. For the binder: 13.5 wt% quartz, 69.2 wt% magnesium calcite, 13.9 wt% montmorillonite, and 3.4 wt% aragonite.

The weight loss percentages have been calculated from the TGA-DSC

Table 1
XRF analyses of the major oxides in mortar samples (in wt%).

Sample	SiO ₂	Al ₂ O ₃	Fe ₂ O ₃	MnO	MgO	CaO	Na ₂ O	K ₂ O	TiO ₂	P ₂ O ₅	SO ₃	L.O.I.	Total
01	45.42	1.30	0.70	0.39	0.66	27.93	0.09	0.29	0.05	0.20	0.18	22.78	100.00
02	63.03	1.85	0.66	0.05	0.99	17.00	0.11	0.38	0.07	0.12	0.12	15.60	100.00
03	50.44	2.12	0.98	0.16	0.65	24.25	0.13	0.46	0.11	0.19	0.11	20.39	100.00
04	35.27	8.83	2.80	0.56	0.82	25.92	1.11	2.19	0.22	0.28	0.10	21.88	100.00
05	53.58	2.27	1.07	0.15	1.40	21.65	0.12	0.34	0.14	0.10	0.10	19.06	100.00
06	31.15	7.03	5.66	1.17	2.87	27.36	0.30	0.62	0.44	0.30	0.10	23.01	100.00
07	42.12	11.29	5.04	0.36	2.06	19.16	0.86	1.68	0.51	0.18	0.11	16.64	100.00
08	50.94	0.94	0.75	0.16	1.11	25.26	0.12	0.20	0.06	0.06	0.28	20.13	100.00
09	42.16	0.65	0.49	0.11	0.36	28.86	0.08	0.14	N.D.	0.06	0.11	26.98	100.00
10	26.06	3.80	1.75	0.37	1.04	36.15	0.15	0.42	0.22	0.17	0.21	29.67	100.00

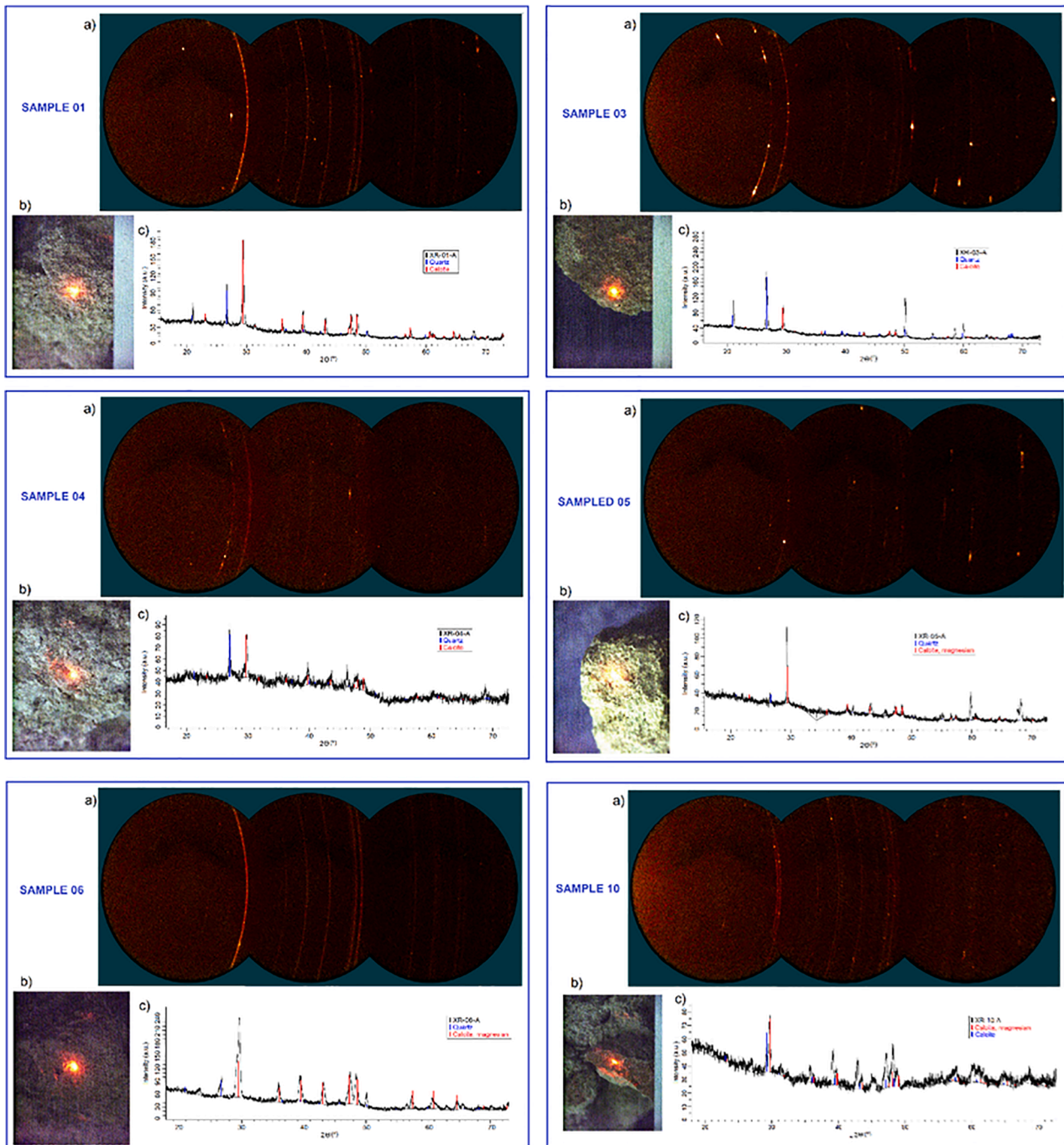


Fig. 5. μ-XRD analysis (selected samples): a) μ-XRD superposed 2D frames, b) area analysed highlighted with laser, and c) integrated diffractogram.

Table 2
μ-XRD results of mortar samples (*indicates different analysis points in the same sample).

Sample	RIR method results		composition	comments
	calcite (wt%)	quartz (wt%)		
01	90	10	calcite + quartz	quartz: non-homogeneous rings (large crystallites)
02			calcite + quartz	
03			calcite + quartz	
04			calcite + quartz	
05			magnesium	
06	98	2	calcite + quartz	
07	90(p1*)	10(p1*)	magnesium	
08	15(p2*) 98(p1*)	85(p2*) 2(p1*)	calcite + quartz	amorphous material with some crystalline calcite
09	(p2*) 52(p1*) 100 (p2*)	(p2*) 48(p1*)	calcite + quartz Calcite	
10		100 (p1*)	Quartz	
	93(p2*) (p3*)	7(p2*) (p3*)	calcite + quartz calcite + magnesium calcite	reddish rock

curves, analysing the following selected temperature ranges, as is usually done in similar studies (e.g., [2,28,29,49,50]): (i) 30–120 °C to detect losses that are due to hygroscopic water, that is, physically adsorbed water; (ii) 120–200 °C range, to detect weight loss related to the water of hydrated salts or gypsum dehydration; and (iii) 200–600 °C to detect the loss of chemically bound water of hydraulic products (i.e.

dehydration of calcium silicates and aluminates hydrates), if there are no other compounds undergoing weight loss (e.g. calcium and magnesium hydroxide, hydromagnesite, organic compounds, etc. [8]); this is the structural bound water (SBW). Above 600 °C, the weight loss could be related to the CO₂ content of carbonated lime, that is, the calcite (CaCO₃) decomposition. And above 700 °C, the weight is not from primary calcite, but from re-carbonated lime [28]. Fig. 8. provides the TGA-DSC curves of the mortars tested (01, 03–07, 09, 10) up to 1000 °C. The TGA signal measures dehydration and the onset of higher temperature decomposition. The DSC shows transitions associated with dehydration and phase transitions.

Hydraulicity is inversely proportional to this ratio: decomposition of carbonates (CO₂-weight loss % above 600 °C) to structurally bound water, SBW (H₂O-weight loss% within the range 200–600 °C) [2,5,28,50,51]. In hydraulic mortars, the SBW is greater than 3%, and in nonhydraulic mortars (i.e. typical lime mortars) the value is less than 3% (and the CO₂ loss over 600 °C is greater than 32%) [27–29,47]. If the CO₂/H₂O ratio is less than 10, the hydraulic nature could be asserted [4,51]. A mortar sample could be classified as highly hydraulic if, after analysing the binary diagram of CO₂/SBW vs. CO₂, the CO₂/SBW ratio is less than 5 and CO₂ is less than 15% [53]. If the ranges are 15–25% for CO₂ and 5–10 for CO₂/SBW ratio, the compounds can be classified as hydraulic or artificial pozzolanic mortars [28,51,53]. These data are depicted in Fig. 9 and Table 4.

Thermal analyses of the whole mortar provide preliminary general data on the hydraulic nature. The most significant weight loss (600 °C, as shown in Fig. 9 and Table 4) could be related to recarbonated lime. It is characterized by a microcrystalline structure and by the thermal decomposition of carbonates from ceramic materials [52]. From the binary diagram of CO₂/SBW vs. CO₂ (Fig. 9, centre), it can be inferred that one of the mortars has the highest hydraulic potential (sample 05), and four samples meet the requirements of hydraulic or artificial pozzolanic materials (01, 03, 09 and 10). As the CO₂/H₂O ratios are less than 10, the hydraulicity can also be presupposed for six samples (01,

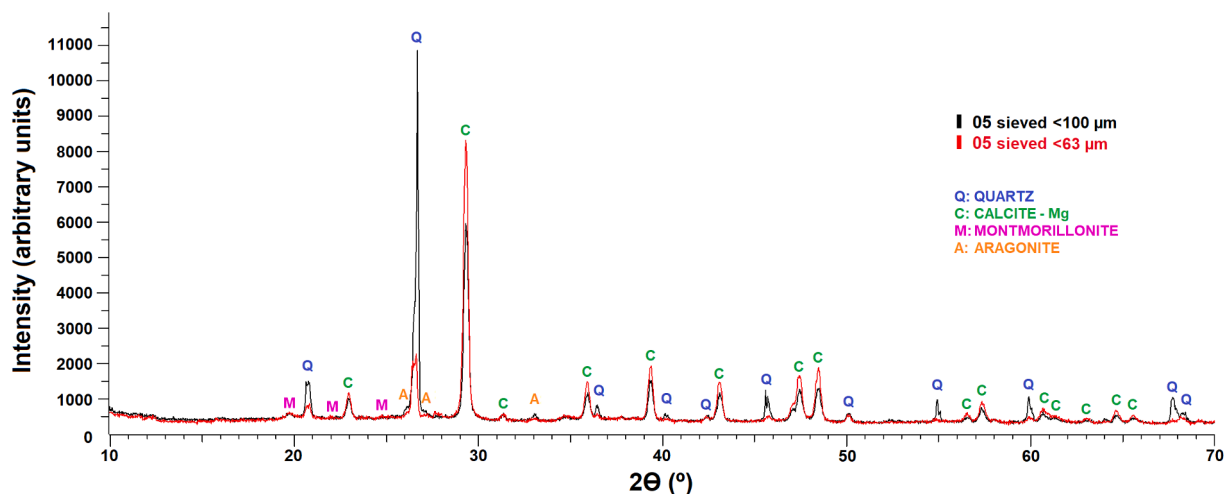


Fig. 6. Sample 05 diffractograms for the whole mortar (sieved less than 100 μm, black line) and the binder fraction (less than 63 μm, red line). The main Bragg peaks of the phases are marked.

Table 3
Phase percentage quantification and Rietveld adjustment data for sample 05 (whole mortar and binder).

Sample	Quartz wt %	Calcite-Mg wt%	Montmorillonite wt %	Aragonite wt %	GOF	R _{wp}	Quartz RBragg	Calcite-Mg RBragg	Montmorillonite RBragg	Aragonite RBragg
05 sieved <100 μm	29.1(9)	49.7(9)	12.7(9)	8.5(6)	2.65	11.37	4.711	4.577	2.922	6.179
05 sieved <63 μm	13.5(2)	69.2(7)	13.9(7)	3.4(5)	1.66	6.42	2.193	2.244	1.557	2.034

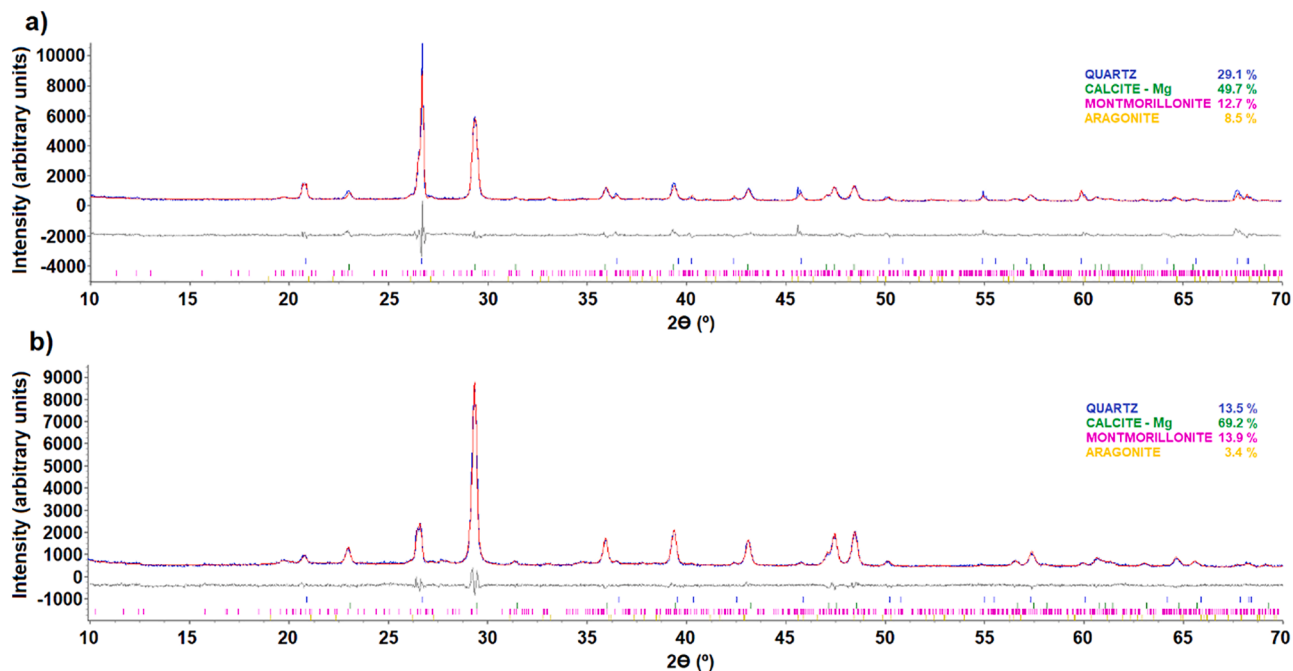


Fig. 7. Experimental diffractograms (blue line) and Rietveld best fit (red): (a) sample 05 (sieved less than 100 μm); and (b) (sieved less than 63 μm). The bottom grey line shows the deviation between the best fit and experimental diffractograms.

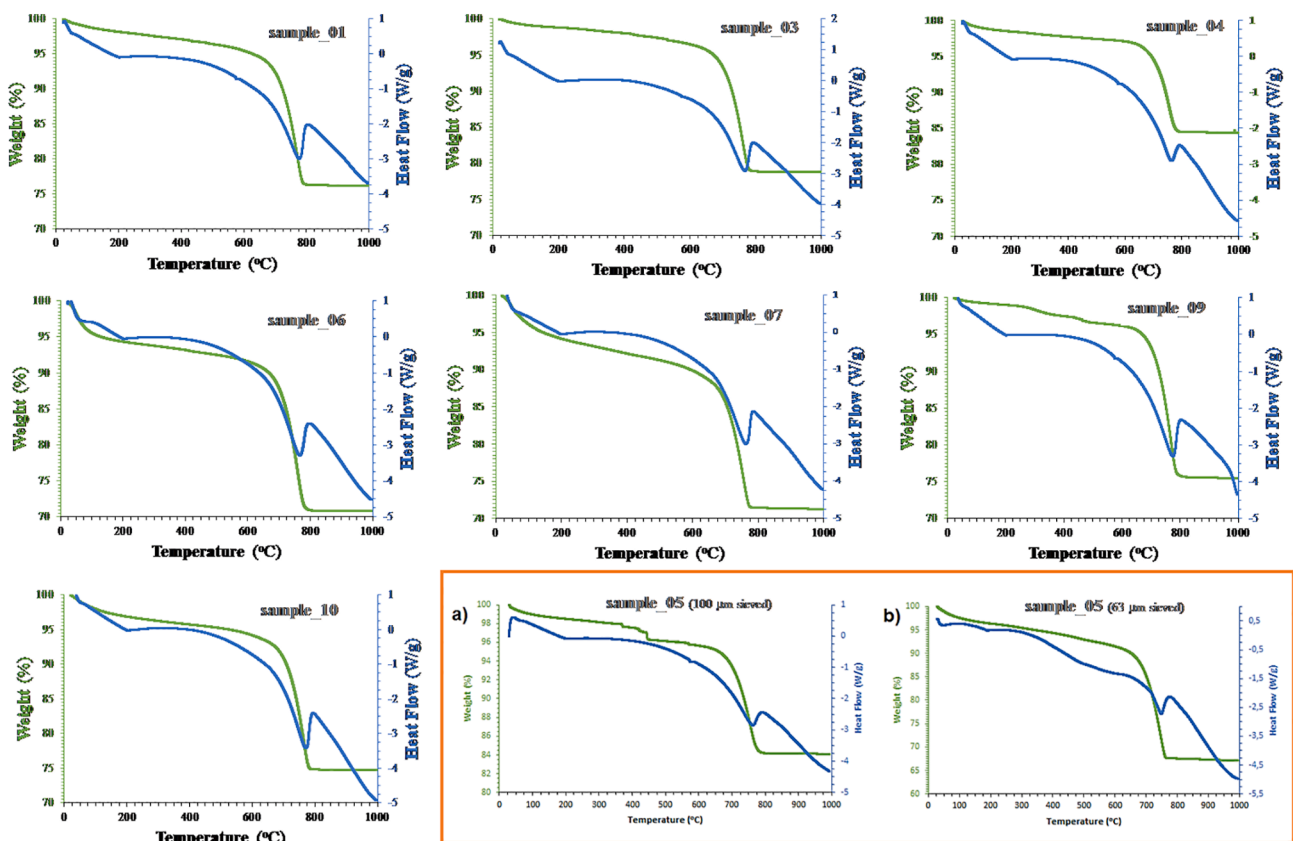


Fig. 8. DSC/TGA curves for selected samples.

03, 05, 07, 09 and 10). In order to distinguish the contribution of lime-binder from carbonate aggregates, the binder and aggregate fractions of sample 05 are analysed. DSC provides similar results for both cases. In TGA, the most remarkable change is the weight loss % obtained by TGA:

(i) 84% loss in total weight once the carbonate decomposes, in the aggregate, and (ii) 68% for the binder. This corroborates the XRD results: lower amount of quartz in the binder, and therefore higher carbonate percentage. In the binder fraction (sample 05 < 63 μm), both the

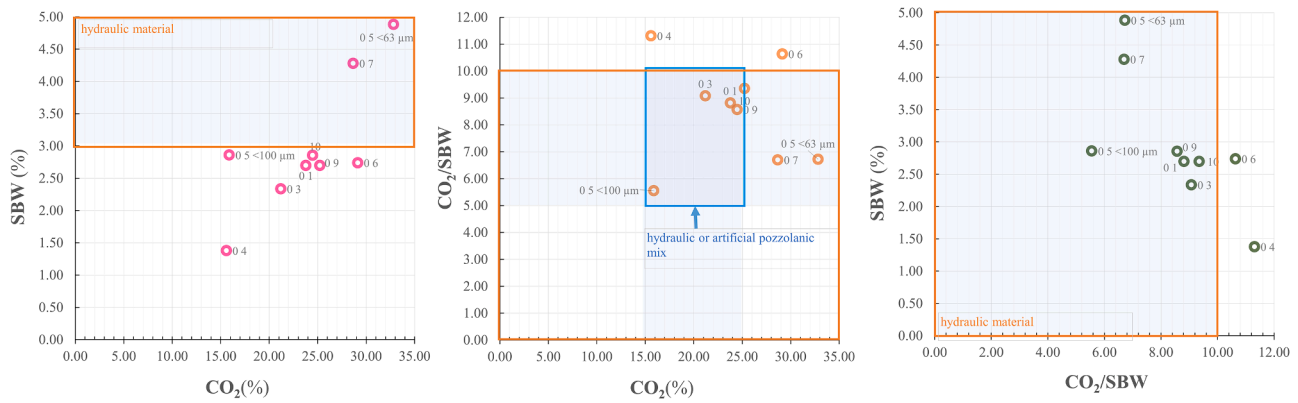


Fig. 9. Thermal analysis: (left) structurally bound water, SBW (H₂O weight loss% within the range 200–600 °C) vs. carbonate decomposition (CO₂-weight loss % above 600 °C); (centre) binary diagram of CO₂/SBW vs. CO₂; (right) structurally bound water vs. CO₂/SBW ratio.

Table 4
Weight loss per temperature range and CO₂/SBW ratio.

Sample	Weight loss per temperature range (%)				CO ₂ /SBW
	30–120 °C	120–200 °C	200–600 °C (SBW)	<600 °C (CO ₂)	
0 1	1.11	0.54	2.70	23.78	8.81
0 3	0.78	0.26	2.34	21.20	9.08
0 4	1.00	0.34	1.38	15.59	11.31
0 5 < 100 μm	1.14	0.33	2.86	15.88	5.55
0 5 < 63 μm	2.73	0.87	4.88	32.82	6.72
0 6	4.39	0.81	2.74	29.13	10.63
0 7	4.04	1.37	4.28	28.67	6.70
0 9	0.56	0.26	2.86	24.47	8.57
10	2.03	0.78	2.70	25.23	9.35

SBW and CO₂/SBW values indicate the hydraulic nature. The aggregates can be directly related to the enhancement of the hydraulicity level (CO₂/SBW vs. CO₂ values for sample 05 fractions (binder and

aggregate)).

From the petrographic images (Figs. 10–12), the samples can be classified into three different groups: medium to fine-grained granular (03 and 05), coarse-grained granular (08), and conglomeratic breccoid (07 and 10). Conglomeratic mortars are more compact and coherent than granular mortars. It is interesting to note that humidity content due to the wet environment, such as that of water-related constructions, could have a beneficial impact on material durability, as it could promote calcite dilution, and the secondary phases formed in the porous volume increase cohesiveness [5]. The aggregates are mainly composed of quartz grains, rock fragments (pumice-type igneous (07 and 10) and sedimentary lithic (03, 05, and 08)) and bioclasts. Ceramic is also detected in some samples. The aggregate size ranges from coarse (rounded shape and, in general, rock) to fine (more angular shape). The binder is carbonated lime-based (calcium carbonate), specifically microcrystalline carbonate less than 4 μm in size (micrite). Opaque minerals (Fe) are also detected. The binder/aggregate ratios are 1/1 (sample 08), 1/3 (sample 03), 1/2 (sample 05) and 1–2.5 for samples 07 and 10 (although in some areas, as a higher aggregate content is detected, the ratio is around 1/3).

The SEM-EDS results are consistent with those of the μXRD and XRF

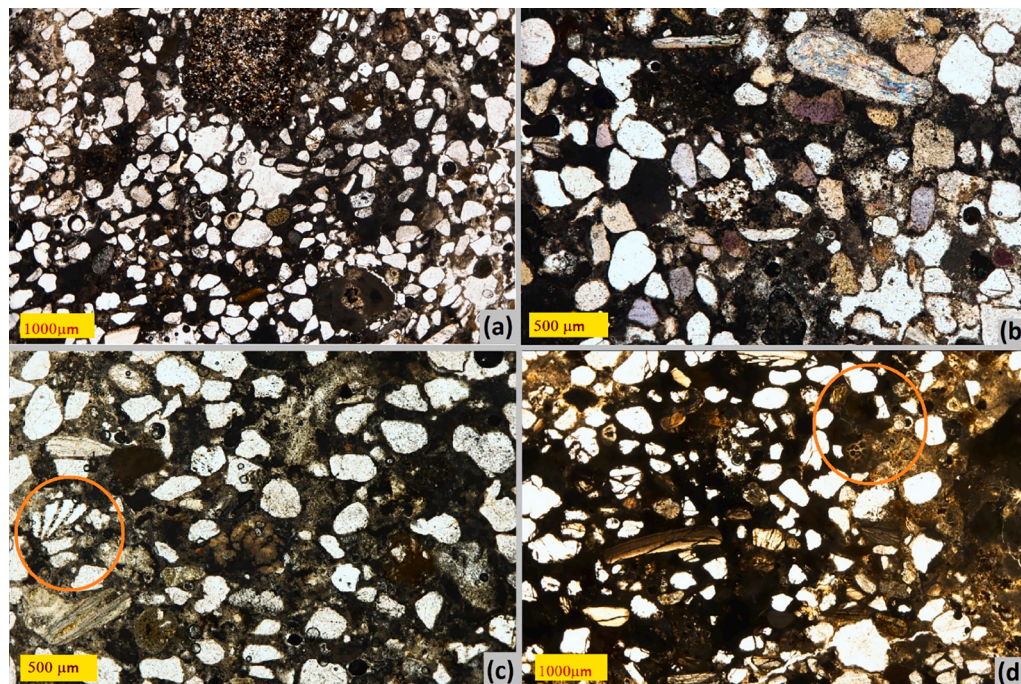


Fig. 10. Fine-grained granular mortar microphotographs: (a) Sample 03, general 2x view, plane-polarized light; granular texture with low compactness and coherence; rock fragment in the central top area. (b) Sample 03, 4x cross-polarized light; subrounded quartz aggregates of variable size (from medium to fine) that are in contact. (c) Sample 03, 4x plane-polarized light; details of bioclasts, bivalves, and opaque minerals. (d) Sample 05, 2x plane-polarized light; low compactness and coherence; subrounded and rounded quartz aggregates floating within a carbonated matrix; details of gastropod bioclasts and algae.

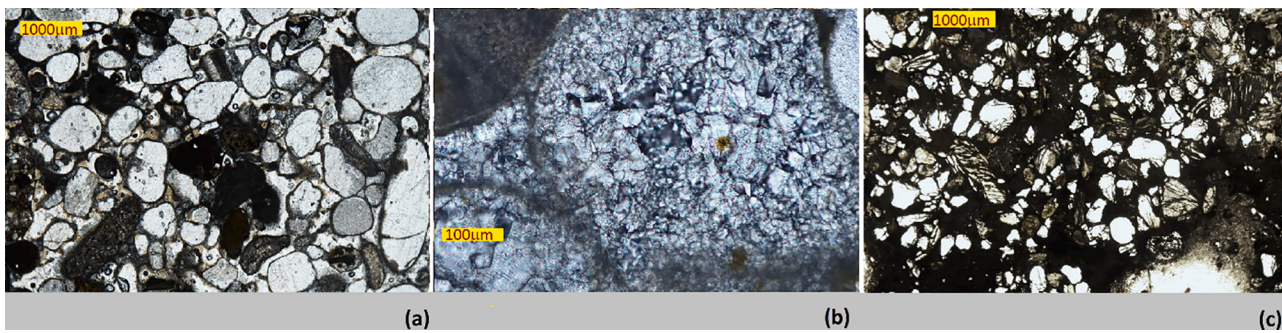


Fig. 11. Coarse-size grained granular mortar microphotographs, sample 08: (a) 2x plane-polarized light, general view of the lower binder/aggregate ratio area; rounded quartz aggregates in contact of similar size. (b) 20x plane-polarized light; details of the espartic cement. (c) 2x plane-polarized light, general view of the higher binder/aggregate ratio area; the aggregates are mainly composed of more heterogeneous size grains (subrounded shape for the smaller ones and reworked for the coarser one); the binder is a micritic matrix with lithic fragments.

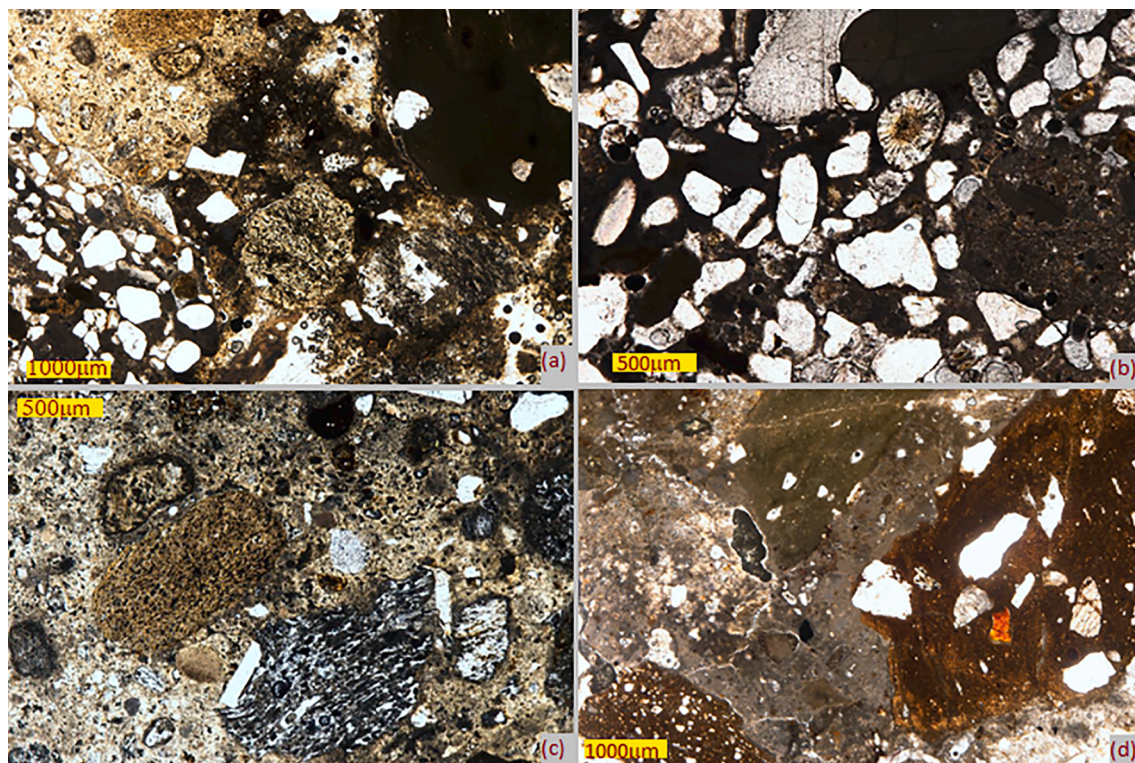


Fig. 12. Conglomeratic-breccoid mortar microphotographs: (a) Sample 07, 2x detail of ceramic fragments (right top corner) lithic fragments (left top corner, and central area) and binder. (b) Sample 07, 4x plane-polarized light; details of algae bioclasts and foraminifera. (c) Sample 07, 4x plane-polarized light; details of pumice-type lithic fragments within the carbonated matrix with abundant quartz clasts; the binder is a micritic matrix with lithic fragments. (d) Sample 10, 2x plane-polarized light; ceramic and rock fragments and carbonated cement.

analyses. Thus, in sample 03 the main elements are Ca and Si, and calcite crystals are detected in the area marked 1 (Fig. 13(a)). These results are in good agreement with the μ XRD analysis where mainly calcite and quartz were observed. In area 2, an elemental composition of Ca, Al, and Si is detected, which is consistent with the C-A-S-H gel [16–18]. In sample 05, Ca is the main element that appears together with Mg in less quantity and Si with Al in some areas (Fig. 13(b)). As in sample 03, this composition is compatible with the calcite and quartz detected in the μ XRD and XRF analyses. The large crystals marked 1 are basically made up of magnesium calcite. The area marked with 2 also has a high proportion of quartz and a higher proportion of Al than area 1. From the EDS mapping of sample 05, the mortar is composed mainly of Ca and Si (Fig. 14). Ca is directly associated with Mg, which is distributed in the same areas. This is consistent with the presence of magnesium calcite, which is consistent with the XRD and μ -XRD analyses. Si is distributed

mainly in areas with a lower Ca content and corresponds to quartz. However, Al is found in a much lower proportion in general in sample 05, as expected from the results obtained by XRF in the ground sample.

From the compositional and thermal characterization, the main remarks can be summarized as follows:

- The main chemical elements are Ca and Si, and the compounds are calcite and quartz. From the high amount of Ca, it can be concluded that the materials are lime mortars; recarbonated lime with a microcrystalline structure (micrite) is detected in the samples. The Si content is due to the use of quartz sand; the presence of bioclasts confirms that the aggregate is sea sand. Ceramic fragments are detected both visually and experimentally (thermal decomposition of carbonates and C-A-S-H gel from the lime/pozzolanic material reaction).

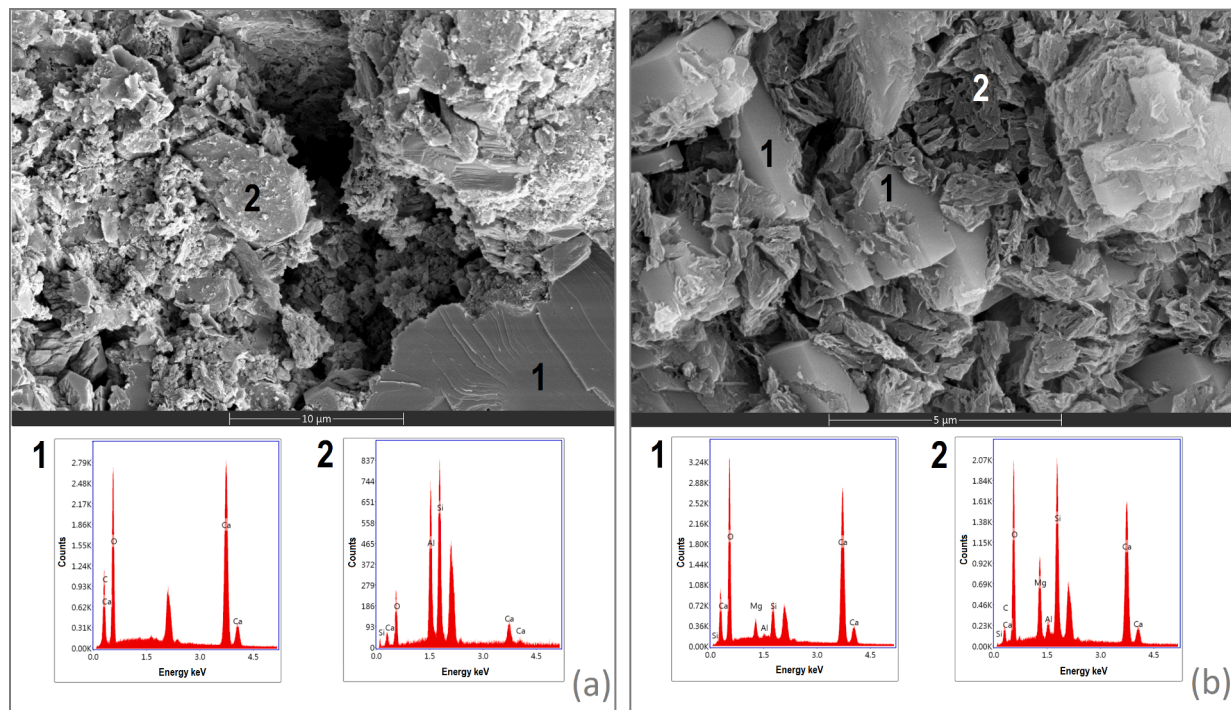


Fig. 13. SEM-EDS analysis (micrographs and EDS): (a) sample 03; (b) sample 05.

- From the $\text{CO}_2/\text{H}_2\text{O}$ ratios and the SBW values, the hydraulicity can be presupposed (except for two samples). The CO_2/SBW vs. CO_2 diagrams show that one of the samples exhibits the highest hydraulic material (mortar from the settling tank), and four more samples meet the requirements of hydraulic or artificial pozzolanic materials (mortars from the drop shaft, settling tank, water tower, and bearing wall of the channel). The C-A-S-H gel also confirms the presence of hydraulic phases.
- The binder/aggregate ratios and petrographic classifications are variable, and they are not constant within the samples of the same group: 1/1 and coarse-grained granular (structural mortar of the bearing wall), 1/3 and medium to fine-granular (drop shaft), 1/2 and medium to fine-granular (settling tank), 1/2.5–1/3 and conglomeratic-breccoid (channel), 1/2.5–1/3 and conglomeratic-breccoid (water tower).
- The sea sand content could be associated with worse material behaviour and durability. The sample with the worst hydraulic level (mortar from the channel) has the highest fine aggregate content.
- Microstructure and physical properties analysis (pore system, morphology, density, and surface area)

As far as microstructure and physical properties are concerned, the experimental campaign has provided relevant qualitative and quantitative complementary data. The computed tomography (CT) together with the SEM images and microphotographs gives qualitative data on the mortar microstructure (e.g., morphology, pore system and crack pattern) that are complemented with the quantitative data obtained from the MIP, physisorption and pycnometry analyses (mass, intrusion volume, apparent volume, real density, bulk density, pore size, pore volume, total porosity and BET surface area), Table 5. These data can be linked to both durability features and manufacturing techniques, and will be discussed in detail in the following paragraphs.

In CT images, the darkest zones are the minor density areas (pores), and the whitest zones are those of the highest density (aggregates). The intermediate tone areas are related to the binder matrix. As can be observed in Fig. 15, the coarser pores could be attributed to entrapped air and/or inadequate compaction during placement. These types of

pores are irregular in shape and distribution, and they are formed during the mixing process. If, during placement, an adequate mechanical treatment (tooling) is applied, the air content is reduced [13]. The amount of water used during manufacturing also has an impact on the formation of entrapped air pores; very dry mortars are more prone to present entrapped air pores than wetter mortars. Spherical pores could be due to bubble formation by water release during manufacturing [11], and in historical waterproofing mortars, the porous system consists mainly of this type of pores [5]. The cause of the inner cracks (for example, those observed in Fig. 16 near the yellow arrows) could be the drying shrinkage. These cracks, which are more common in mortars with a high water content, are related to the use of small-size aggregates. Although environmental conditions during hardening also have an impact on shrinkage cracking (if the humidity level decreases, the cracking increases) due to the location of the ensemble, those cracks could be linked to the aggregate size (sand) and to the water content. Both entrapped air and shrinkage cracks increase the water permeability, reducing the mechanical performance. If no cracking is observed within the matrix, a soft burning manufacturing procedure could be assumed. When the pore size distribution is analysed, it can be elucidated whether the total porosity is related to the coarsening of pores or to the increase in pore number. In general, the worst situation in terms of material damage and durability can be attributed to an increase in pore size [13]. CT images show that although the number of irregular-size macropores is not too high, they could worsen the weakness of the material.

It is important to point out that the tomography images match the density analysis data presented in Table 5, as the sample with the highest bulk density exhibits shrinkage cracks (sample 03). The higher the bulk density value, the higher the shrinkage, and minor chemical reactivity could be expected [16]. On the contrary, high density values could be an advantage from a structural point of view, as, in historical mortars, higher density is related to better mechanical performance [54]. In sample 03, the bulk density is approximately 37% higher than that of the other samples. Higher bulk density values could also be associated with the use of crushed brick within the matrix [28]. When brick fragments are added to the mix, lime penetrates the ceramic

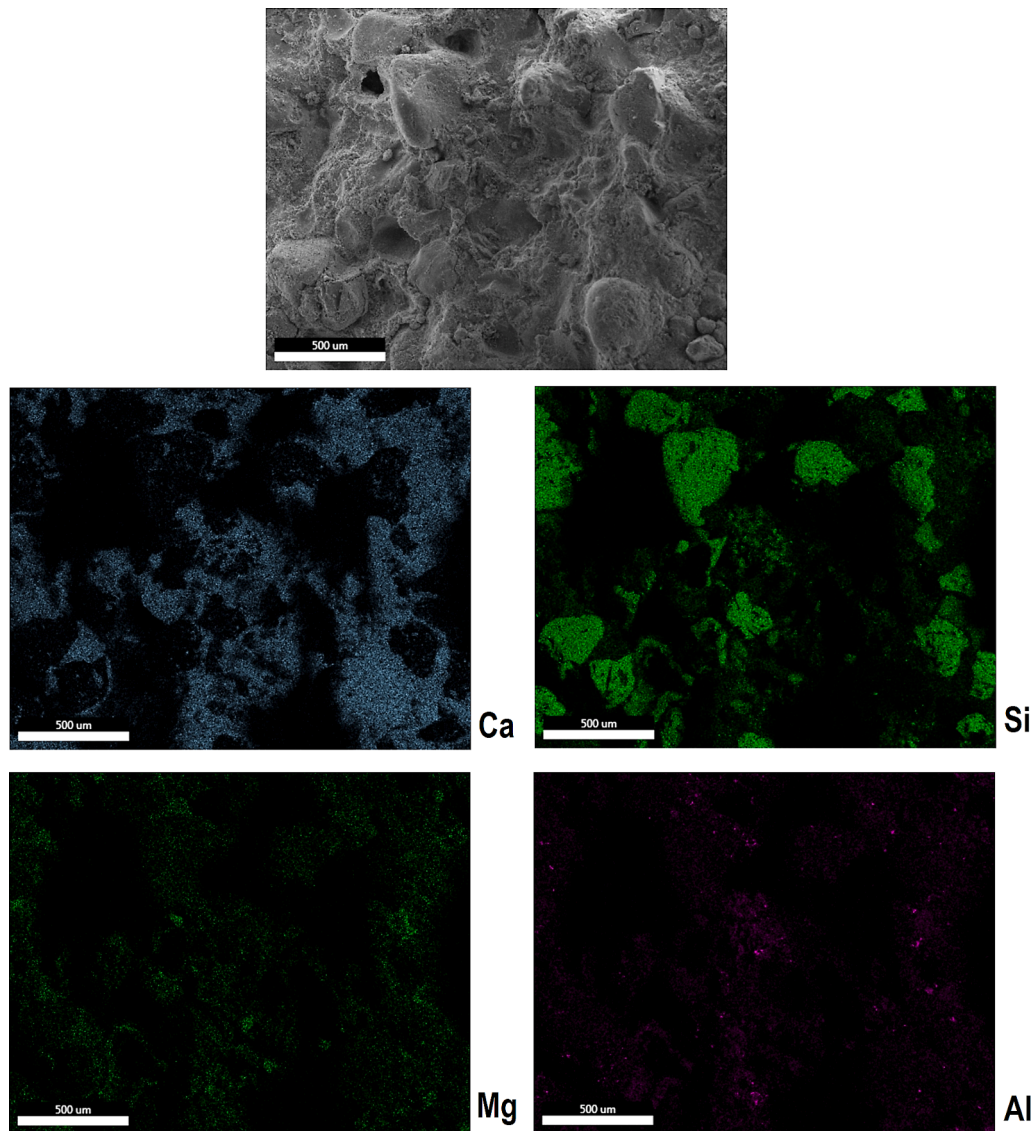


Fig. 14. SEM-EDS analysis (micrographs and EDS-mapping) of sample 05.

Table 5
Physical properties characterization.

Sample	BET surface area (m ² /g)	Real density (g/cm ³)	Bulk density (g/cm ³)	Total porosity (%)	*Average Pore diameter micro-meso range (μm)	*Cumulative pore volume micro-meso range (cm ³ /g)	**Average Pore diameter meso-macro range (μm)	**Cumulative pore volume meso-macro range (cm ³ /g)
03	6.68	2.68	2.21	17.46	0.008	0.01	0.77	0.08
04	11.63	2.7	1.62	39.95	0.006	0.02	0.93	0.25
05	20.66	2.65	1.57	41.02	0.006	0.03	0.95	0.26

fragments, and the ceramic structure is transformed by a reaction that reduces the pore size and increases the density. In these mortars, the highest bulk density is that of the material that has opaque minerals and rock fragments. In the samples, the real density is quite similar, ranging from 2.56 to 2.70 g/cm³ in eight samples (01, 03–07, 09, and 10). These values, which can be related to the aggregate granulometry, could be attributed to a high proportion of fine sand. The presence of ceramic fragments does not cause a remarkable variation in the real densities

that have been obtained.

The CT images provide interesting data on the interface contact area in terms of durability and mechanical strength. The interface plays a critical role in moisture transport, as it can be assumed that there is no perfect hydraulic mortar in the unit-mortar joint [55]. In this type of mortar, the lack of coarse aggregate and carbonation at the interface could create a moisture barrier [13]. Although large-size aggregates are observed in some interface zones (Fig. 16, sample 03 bottom), no

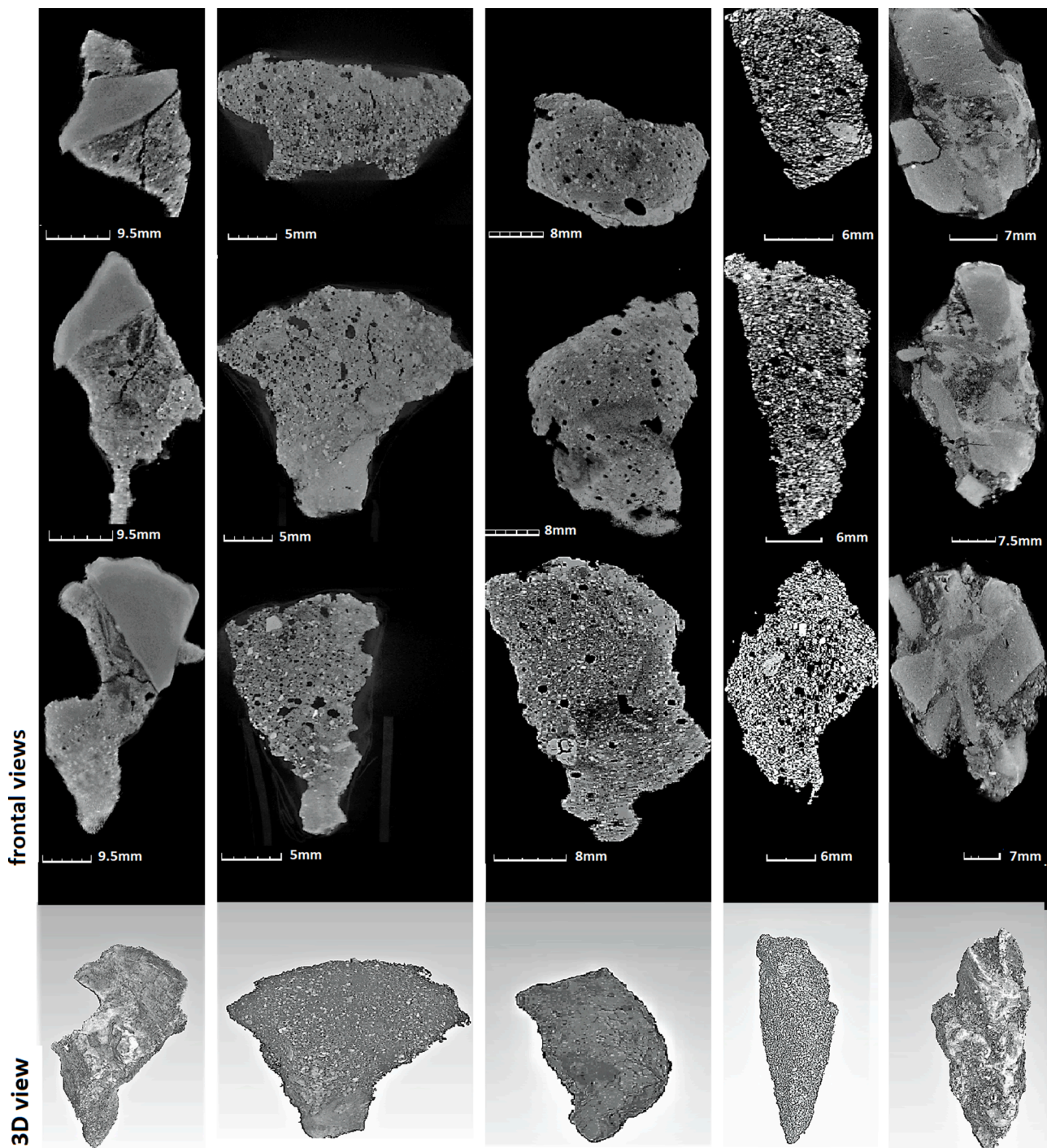


Fig. 15. Computed tomography images of selected samples (01, 03, 04, 05, and 06 from left to right): 3D view and frontal view.

detachment between materials is detected in the joint areas, and the bond could be classified as satisfactory. In Fig. 17, neither large-size pores nor cracking are detected, but less dense matrix areas are located near the joint. These less dense areas could affect the mechanical performance, although mechanical characterization would be necessary to confirm it.

Regarding the total porosity percentage, samples 04 and 05 present the highest values (39.95 and 41.02, respectively) and, comparatively, that of sample 03 is significantly lower (around 56% less). These values match the density analyses, since the density is inversely proportional to porosity. Samples 04 and 05 can be classified as high total porosity materials, as the common reference threshold value of 20% is widely

exceeded [13]; and only one sample, sample 03, can be classified as a dense structure mortar. Since in this type of materials a total porosity increase results in a compressive strength decrease, it could be assumed that sample 03 has more adequate porosity values for a better structural performance (although mechanical tests would be necessary to corroborate the aforementioned). When comparing the density and porosity values, the porosity data exhibit higher variation, and the densities are more similar. This variation could be attributed to the composition of the binder and the binder-aggregate ratio [56].

The BET surface area values range from 6.68 to 20.66 m²/g. In the samples, a higher BET surface area is related to a higher pore volume, but not to a larger pore size (as can be observed in sample 05). Higher

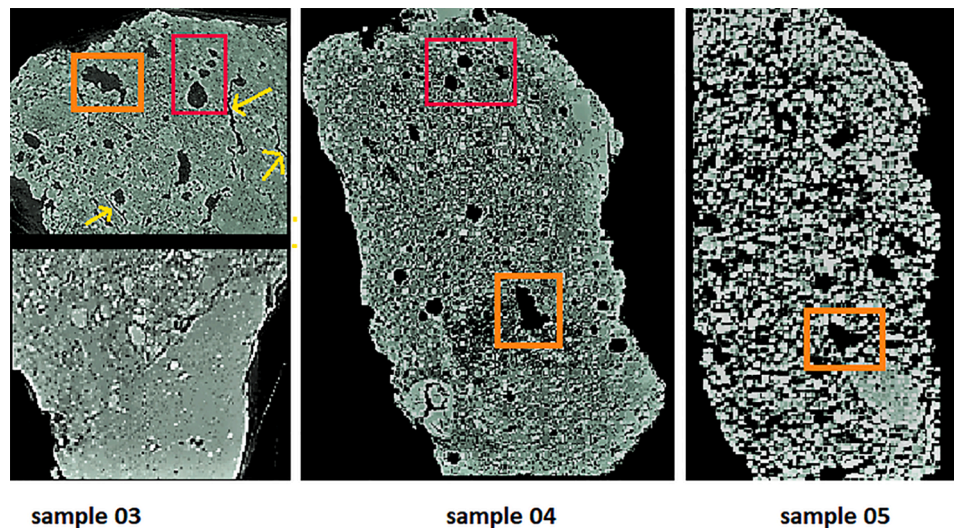


Fig. 16. Computed tomography images. Microstructure details (samples 03, 04 and 05, from left to right): shrinkage cracking (yellow arrow), bubble formation by water release (red rectangle) and air-entrapped pores (orange rectangle) examples.

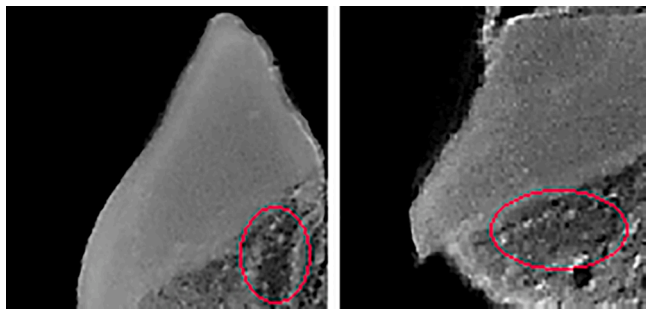


Fig. 17. Computed tomography images. Microstructure details showing the less dense area near the interface (sample 01).

BET surface area (such as that of sample 05) could indicate a higher proportion of clay minerals due to the presence of brick fragments [57]. Low specific surface values are associated with a high lime content and a broad porosity range [11].

In addition to the qualitative analysis of the microstructure, the performed MIP and physisorption tests enrich the knowledge of different durability and manufacturing features by analysing the pore size distribution. As mentioned above, the results from both tests must be considered as complementary, as MIP provides reliable data within the meso and macro ranges, and physisorption is especially useful for analysing the micropore range. Figs. 18 and 19 depict the percentage of pores with a specific size, as well as the percentage of porous volume occupied by each pore size. To classify the pore size, the criteria are those defined by IUPAC [58]: macro ($>0.05 \mu\text{m}$), meso ($0.002\text{--}0.05 \mu\text{m}$) and micro (less than $0.002 \mu\text{m}$).

It must be taken into account that because of the characteristics of the tests (MIP and physisorption) the measured pores are those that are interconnected to each other and to the outer side. These data are relevant from a durability point of view, especially in terms of water permeability. In the *meso*-macro pore range, the percentage of porous volume is distributed in each sample as follows (Fig. 18): (i) sample 03: 78.65% macropores, 21.35% mesopores; (ii) sample 04: 79.79% macropores, 20.11% mesopores, and (iii) sample 05: 77.18% macropores, 22.82% mesopores. Although the porous volume is mainly dominated by the macropore volume, most of the pores are meso, as can be deduced from the percentage of the number of pores vs. the pore size distribution. The percentage of number of pores vs. pore size distribution is: (i)

sample 03: 99.79% of pores range between 0.004 and $0.05 \mu\text{m}$ and 0.21% between 0.05 and $10 \mu\text{m}$; (ii) sample 04: 99.24% of pores range between 0.004 and $0.05 \mu\text{m}$ and 0.76% between 0.05 and $10 \mu\text{m}$; and (iii) sample 05: 99.68% of pores range between 0.004 and $0.05 \mu\text{m}$ and 0.32% between 0.05 and $10 \mu\text{m}$. Fig. 19 provides these results for the micropore range: (i) sample 03: 0.51% micropores; (ii) sample 04: 0.22% micropores; and (iii) sample 05: 0.33% micropores. In that range, the percentage of the number of pores vs. pore size distribution is: (i) sample 03: 27% have a diameter less than $0.002 \mu\text{m}$; (ii) sample 04: 18% have a diameter less than $0.002 \mu\text{m}$; and (iii) sample 05: 19% have a diameter less than $0.002 \mu\text{m}$. The volume of the micropores could be due to the sand used as a raw material.

The role of porosity is essential in mechanical performance, despite the type of binding system [5] and small pore size and low porosity are desirable. The pore size is also related to durability, as pore dimensions should be large enough to prevent condensation inside structural elements (a small pore has a water condensation effect) and, at the same time, small enough to provide a water-proof barrier [11]. Moreover, an adequate pore size favours the entry of air and, therefore, carbonation, preventing the crystallization of salts. As a reference to assess durability, the following values can be adopted for the pore diameter [11,17]: $0.01\text{--}0.2 \mu\text{m}$ (within the meso and macropore ranges) is not detrimental to durability, and $2\text{--}20 \mu\text{m}$ (within the macropore range) can promote weathering. Analysing the porous volume distribution of the samples, the percentage within the weathering range is as follows: 3.30% in sample 3, 12% in sample 4, and 10% in sample 5 (data from the MIP). Furthermore, if the pore diameter is significantly high (greater than $50 \mu\text{m}$) this could be due to a bad cohesion between the binder and the aggregate [59]. In the samples, no value exceeds the limit value of $50 \mu\text{m}$. Farci et al. [60] also provide interesting reference values that were obtained from the characterization of mortar samples from Roman water supplies: If the lime-based binder and the crushed fictile have a significant fraction of pores with a diameter less than $0.01 \mu\text{m}$ and if the total porosity is less than 25% , the materials are relatively water resistant. In the samples analysed, the total porosity of sample 03 (17.46%) matches that threshold value (36% of the porous volume has a diameter smaller than $0.01 \mu\text{m}$).

The pore size is directly related to a durability factor, the water permeability (i.e., the larger the pore size, the greater the permeability to water and vice versa). It is convenient to have a size less than $100 \mu\text{m}$, since pores larger than $100 \mu\text{m}$ promote water permeability through gravity or wind-driven water ingress [13]. The samples satisfy the aforementioned condition, as the maximum pore size measured is 10.6

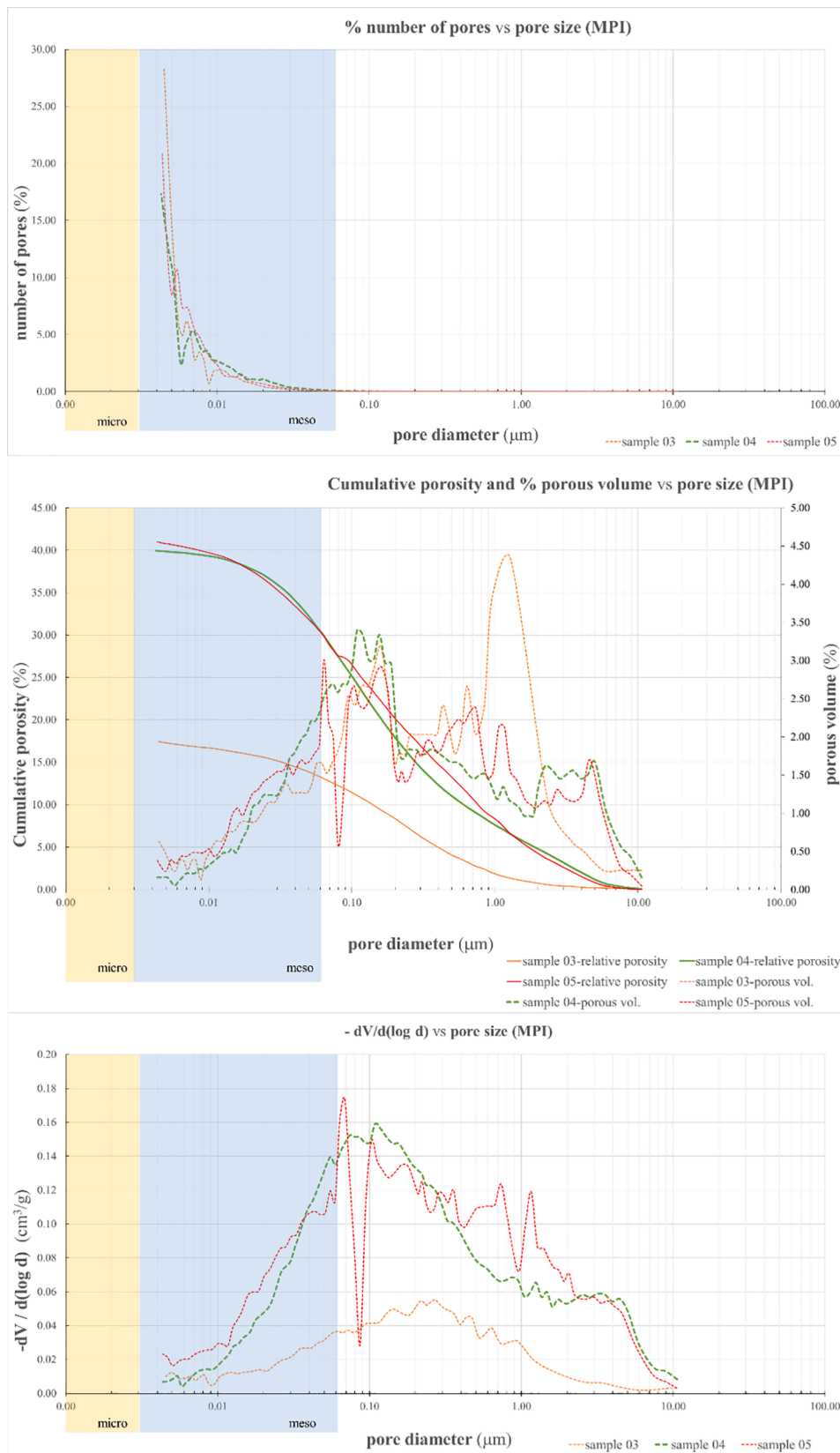


Fig.18. MIP analysis: (top) percentage of pores with a specific size; (centre) cumulative porosity, percentage of porous volume occupied by each pore size and relative porosity; (bottom) $-dV/d(\log d)$ vs. pore diameter, V = volume and d = diameter.

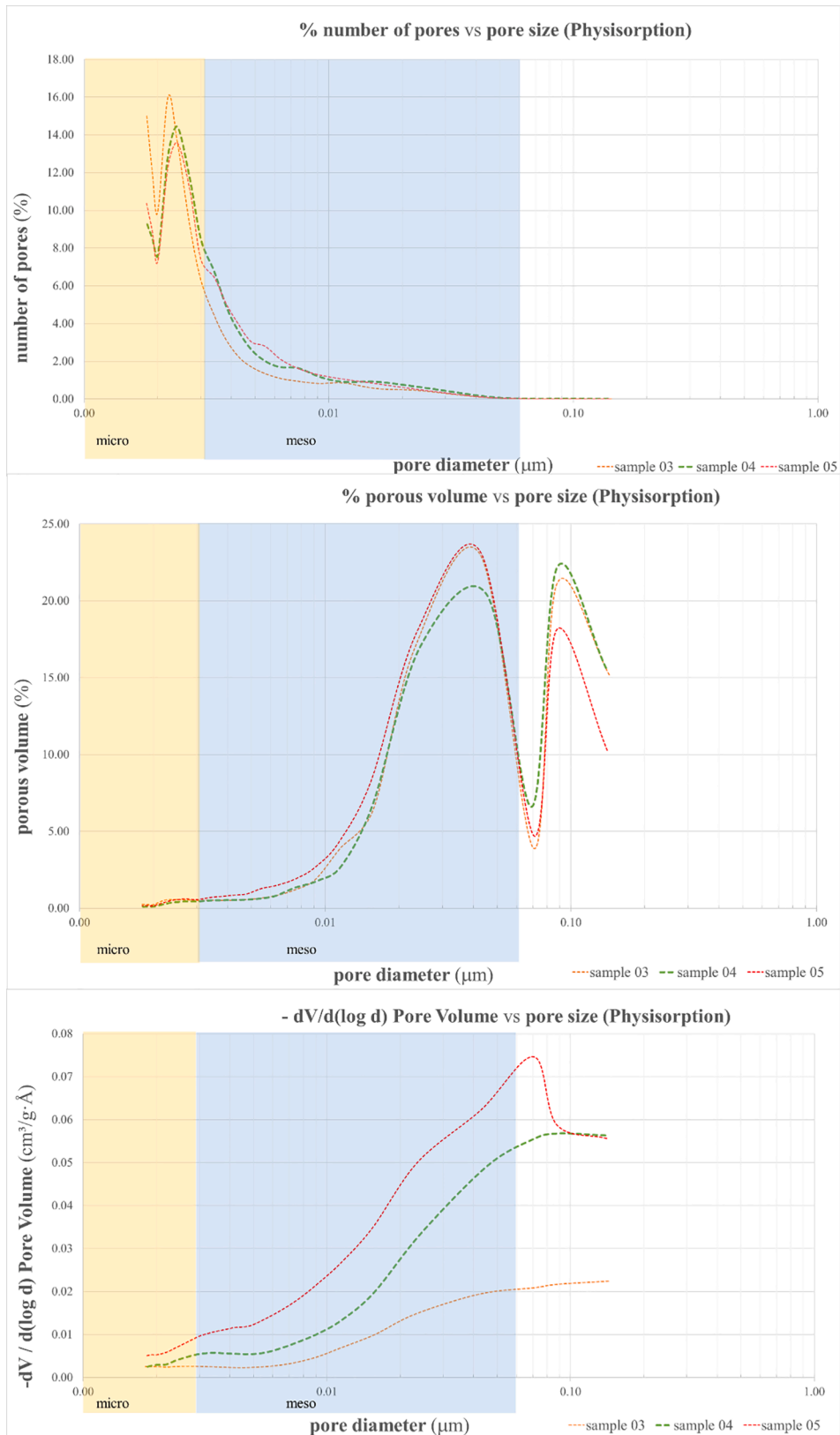


Fig. 19. Physiorption analysis: (top) percentage of pores with a specific size; (centre) percentage of porous volume occupied by each pore size; (bottom) -dV/d(logd) vs. pore diameter, V = volume and d = diameter.

µm. This feature is essential in this ensemble, as Baelo Claudia is located in a windy coastal area with a high humidity content.

In addition to the mechanical performance and durability characteristics, the total porosity and pore size distribution can be related to the type of mortar as follows [13]: (i) in lime-sand mortar, the total porosity is greater than 20% and a small quantity of pores has a size less than 1 µm; (ii) in friable and altered mortar, the total porosity is much greater than 20% and coarser pores are observed; and (iii) in hydraulic mortar, the total porosity is low and more fine pores are within the inner matrix. According to that classification, only one sample matches the porosity limit value of the hydraulic mortar (sample 03), and the others better match the values of the deteriorated material. However, in the samples, the high number of pores with a diameter less than 1 µm indicates the presence of a hydraulic lime phase. The average pore diameter is also a key factor in determining the type of mortar: in high hydraulicity level waterproofing mortars, the pore size is less than in those with a lower level [4], and the diameter ranges between 0.1 and 1 µm, with an open porosity between 12 and 20% [5]. Although the average diameter ranges achieve the aforementioned (0.77–0.95 µm), since the open porosities are higher (around 60%) the waterproof level could not be too much higher.

From the analysis of microstructure and physical properties, the main remarks can be summarized as follows.

- The porous system consists mainly of spherical pores, which are common in waterproofing ancient mortars; those pores can be associated with the bubble formation by water release during the manufacturing. The high number of pores with a diameter less than 1 µm is evidence of a hydraulic lime phase within the matrix. The

average diameter (0.77–0.95 µm) is typical of high levels of hydraulicity. The maximum pore diameter value (10.6 µm) achieves the reference limits that indicate a water ingress risk reduction (100 µm), and an adequate binder-aggregate cohesion (50 µm). The porous volume within the weathering range (2–20 µm) is quite low (3.30–12%), and the minor values are for the mortars with high hydraulic potential (samples 03 and 05, from the drop shaft and the settling tank). However, the high value of open porosity (around 60%) reduces the waterproofing properties. From the total porosity and porous volume values (17.46% and 36% of the porous volume with a diameter less than 0.01 µm, respectively), the water-resistant properties of one of the mortars (sample 03) can also be presupposed; the other samples can be classified as friable materials. Coarse and irregular (in shape and distribution) entrapped air pores have been identified. Both inadequate compactation and tooling during placement are the more probable origin of those pores.

- Although some large-size aggregates are detected at the interface, no detachment is observed between the structural materials (mortar/stone).

Fig. 20 summarizes the main findings from the experimental campaign in relation to durability and manufacturing techniques.

To contextualize the mortars, Table 6 allows a comparison among the main physical properties of the analysed materials and Roman mortars from water-related and/or coetaneous buildings analysed in recent research works during the last 10 years [5,9,11,15,54,57,17,57–63].

In the reviewed works, the real density values are quite similar among them, ranging from 2.37 to 2.74 g/cm³ (only a higher value was

Data											Building techniques		Durability			
											materials, manufacturing		improvement		worsening	
											no inner cracking*	→ soft-burned manufacturing	→ less transfer paths for damage agents	better mechanical resistance		
			+								inner shrinkage cracking	→ small size aggregate	→	more transfer paths for damage agents		
											coarse irregular pores	→ high water content	→	worse mechanical resistance		
											water release spherical pores	→ deficient compactation	→	permeability increase		
											porosity decrease at interface	→ hydraulic mortar	→ waterproof material	worse mechanical resistance		
											no detachment at interface	→ adequate compactation	adequate bond between materials			
											large-size aggregate at interface	→ adequate tooling	CO ₂ barrier			
												→ irregular aggregate size	→	permeability increase		
														worse mechanical resistance		
											quartzitic grain	sea sand as fine aggregate; sea shell can reduce workability		deterioration due to chloride content		
											bioclasts (bivalves, algae, gastropod, foraminifera)	→				
											pumice-type lithic fragment	→	better mechanical resistance			
											rock fragment	→				
											opaque minerals (Fe)					
											ceramic fragments					
											carbonated matrix					
											binder/aggregate	→ binder/aggregate: 1/2-1/3				
											high bulk density	→	→ better mechanical resistance	more shrinkage(permeability increase)		
											real density ranging from 2.5-2.7g/cm ³	→ high fine aggregate content	→ better consistency	other resistant raw materials required		
											high total porosity	→	→	worse mechanical resistance		
											low total porosity	→				
											high porous volume with diameter<0.01µm	→ hydraulic lime	→ better mechanical resistance	waterproof material		
											high number of pores with diameter<1µm	→				
											porous volume within the weathering range (2-20µm)	→	→ small volume prone to weathering			
											pore diameter>100µm	→	→ waterproof material			
											high surface area	→ clay material content				
											low surface area	→ high lime content				
											high Si content	→ quartz sand as aggregate				
											high Ca content	→ lime as binder				
											re-carbonated lime	→ ceramic materials	better mechanical resistance			
											thermal decomposition of carbonates	→				
											CO ₂ /SBW <5-10, CO ₂ <15-25%	→ hydraulic mix + pozzolanic	waterproof material, better mechanical resistance			
											CO ₂ /H ₂ O<10	→ hydraulic mix	waterproof material			
											SBW>3%	→ hydraulic mix	waterproof material			
											main elements: Ca and Si	→ quartz sand and lime binder				
											C-A-S-H gel	→ pozzolanic materials	waterproof and better mechanical resistance			

Fig. 20. Experimental results in relation to durability and manufacturing techniques (CT: computed tomography; P: petrography; F: MIP, pycnometry and physiorption, X: X-ray fluorescence, µ-X-ray diffraction; T: thermal analysis; S: SEM-EDS).

Table 6
Main physical properties of Roman mortars in water-related and/or coetaneous buildings.

Reference	Code	Period	Location	Building material type	Real density (g/cm ³)	Bulk density (g/cm ³)	Total porosity (%)	Open porosity (%)	Pore diameter (µm)	Surface area (m ² /g)
*Rispoli et al., 2020	R20	Roman (Augustan rule 27 B.C-14 A.D.)	Cistern, Campi Flegrei, Italy	concretion and coating mortar	2.56	1.72	52.4	0.01-0.2	29.32
*Rispoli, De Bonis, et al., 2019	R19	Roman (2 nd -4 th centuries)	Thermal complex, Baia, Italy	coating mortar	2.37-2.70	1.35-1.58	38.2-49.9	0.2-2
*Laycock, et al., 2019	L19	Roman (2 nd century)	Baths, Wallsend, UK	structural mortar	19.9	2
*Rispoli, Graziano, et al., 2019	Rb19	Roman (1 st B.C-1 st A.D. centuries)	Villa, Napoli-Campania, Italy	bedding mortar	2.74	1.64	40.42	0.01-0.2	24.25
*Tasci and Büke., 2018	TB18	Roman	Bath, Patara, Turkey	structural mortar (masonry: rubble core+ashlar leaves)	1.20-1.97	20-53
			Bath, Xanthos, Turkey	structural mortar (masonry: rubble core+ashlar leaves)	
			Bath, Tlos, Turkey	structural mortar (masonry: rubble+ashlar)	
Ontiveros-Ortega, Rodríguez-Gutiérrez and Navarro, 2016	OO16	Roman(1 st -2 nd century AD)	Platform, Itálica, Spain	structural mortar	2.5, 2.7, 3.93	1.6	0.1-10
*Stefanidou et al., 2014	S14	Roman (29-27BC)	Baths, Nikopolis, Greece	structural mortar	1.86	19.3
		Roman(2 nd -3 rd century AD)	Baths, Dion, Greece	structural mortar	1.94	12.8
*Drdácký, et al., 2013	D13	Roman (27 BC)	Ponte di Augusto, Narni, Italy	structural concrete (three-leaf stone masonry with inner core of cast concrete)	2.64±0.03	1.69±0.05	36±2
				2.60±0.02	1.79±0.18	31±6
				2.59±0.03	1.73±0.06	50±2
				2.51±0.03	1.16±0.08	54±3
*Polat-Pekmezci and Ersen, 2011	PP11	Roman (1 st century)	Bath, Tarsus, Turkey	structural mortars (brick and stone masonry)	1.49, 1.99	36.03, 19.56
				1.57, 1.86	36.22, 15.66	
				1.78	23.52	
*Kramar, et al., 2011	K11	Roman (1 st -4 th centuries)	Bath complex, Mosnje, Slovenia	bedding mortar (floor)	2.61	1.66	36.43	0.08	5.9931±0.0311

*This Table provides the summarized data of the samples that are more related to those of analysed in this research, in terms of building material type and historic period

C: Calcite; D: Dolomite; Car: Carbonate; Q: Quartz; Al: Albite; An: Anorthite; H: Hematite; Ch: Chert; F: Feldspar; K: Kaolinite; M: Muscovite; Di: Diopside; G: Gypsum; V: Volcanic material; Pu: Pumice; AS: Amorphous silica; Tb: Tobermorite; Phi: Phillipsite; Cbz: Chabazite; Sa: Sanidine; Cpx: Clinopyroxene; Pl: Plagiocase; Mca: Mica; Ana: Analcime; Phyl: Phyllosilicate

obtained for a sample, 3.93 g/cm³, and it was attributed to a well-sorted sand content [11]). The values are also comparable to those of the Baelo Claudia mortars (2.56 to 2.70 g/cm³). The bulk densities are also similar

to those of the mortars analysed in this work (1.57–2.21 g/cm³), with values between 1.2 and 1.97 g/cm³. Total porosity values exhibit a wider range of variation, from 12.8 to 53%, a variation that is also

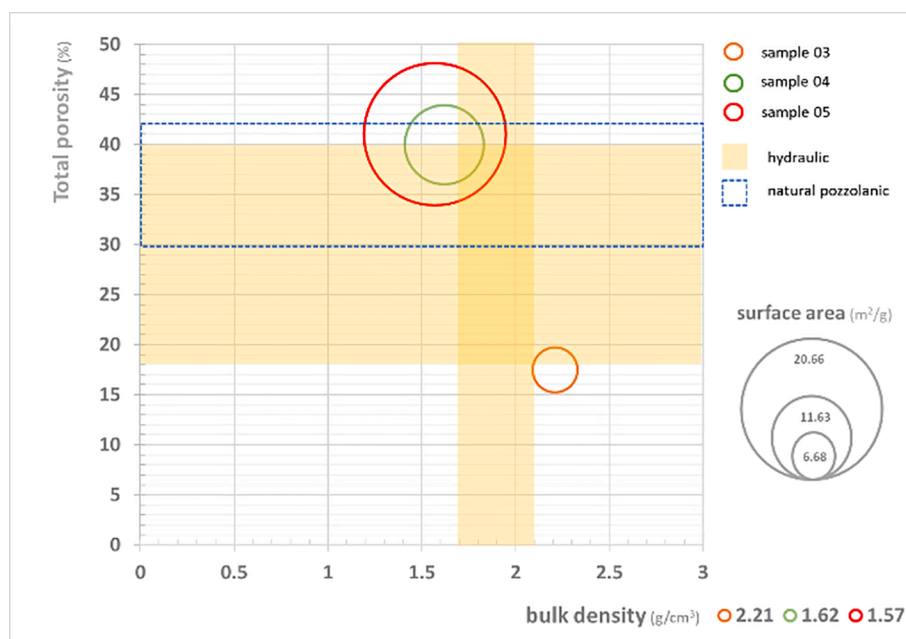


Fig. 21. Mortar classification of the analysed samples from the reference data provided by Moropoulou et al. [64].

observed in this research (17.66–41.02%). Focusing on the pore diameter, although scarce data are obtained from the literature, the most common range is 0.01–2 μm. Thus, most of the pores could be classified as macropores or mesopores. In the reviewed works, MPI is the porosimetry technique that was applied. It is worth noting that neither physisorption nor tomography analyses were applied in the reviewed works to analyse Roman mortars, and therefore the results obtained by these techniques and discussed in this work can enable future in-depth analysis of interest to further progress in the knowledge of Roman mortars. It is worth noting that in Roman mortars the average pore radius is around one order of magnitude smaller than the dimensions of current mortars [10].

According to the reference data provided by Moropoulou et al. [64], from the bulk density, surface area, and total porosity, the categories that correspond better to the mortars analysed are: (i) hydraulic lime mortar for sample 03, and (ii) natural pozzolanic mortar for sample 04. In sample 05, as the value of the surface area is greater than the maximum value provided by those authors (14 m²/g) it is not possible to fully apply that classification. However, in that sample, the more assimilable range is that of the natural pozzolanic mortar (Fig. 21).

Table 7 provides the compositional characterization of Roman mortars from water-related and/or coetaneous buildings [5,9,11,15,54,57,17,57–63]. The Baelo Claudia mortars are quite similar in terms of chemical composition to those of similar constructions. The main differences are observed in sample 02 (higher SiO₂

content and lower CaO) and sample 10 (lower SiO₂ content and higher CaO). These differences could be attributed to a higher amount of aggregate in sample 02 and a higher amount of lime in sample 10.

It is also interesting to analyse the data obtained from the Vitruvian legacy [65]. In Book II, Chapter IV, Vitruvius points out that although it is possible to use sea sand as a raw component (if there are no sandpits from which it can be dug) there are two main problems: (i) it dries slowly, having a detrimental impact on the load bearing capacity, and (ii) when used in walls that are coated with stucco, salty efflorescence is given out which spoils the surface. In the structures, no salty efflorescence were observed. However, the most detrimental impact of sea sand aggregates could be attributed to both their small size and the large amount of water required during manufacturing, resulting in shrinkage cracking (as observed in CT images). If sea sand is used, Vitruvius recommends a binder-aggregate ratio of 1/2 (for pitsand, the proportion is three parts of sand to one of lime). In that case, an additional third part composed of burnt brick (pounded and sifted) increases the quality. In the Baelo Claudia mortars, there were no apparent mortar preparation standards, as the binder-aggregate ratio is quite variable (1/1, 1/2, 1/2.5, and 1/3 from the petrographic analysis). Although microphotographs have shown brick fragments in some samples, the added amount is not constant. Regarding the potential of the “sponge-stone” (pozzolana) to increase strength and allow hardening under water (Chapter VI), pumice-type lithic fragments have also been detected, but as an isolated component and in small quantities. Following on the work by

Table 7
Compositional characterization (%) of Roman mortars from water-related and/or coetaneous buildings.

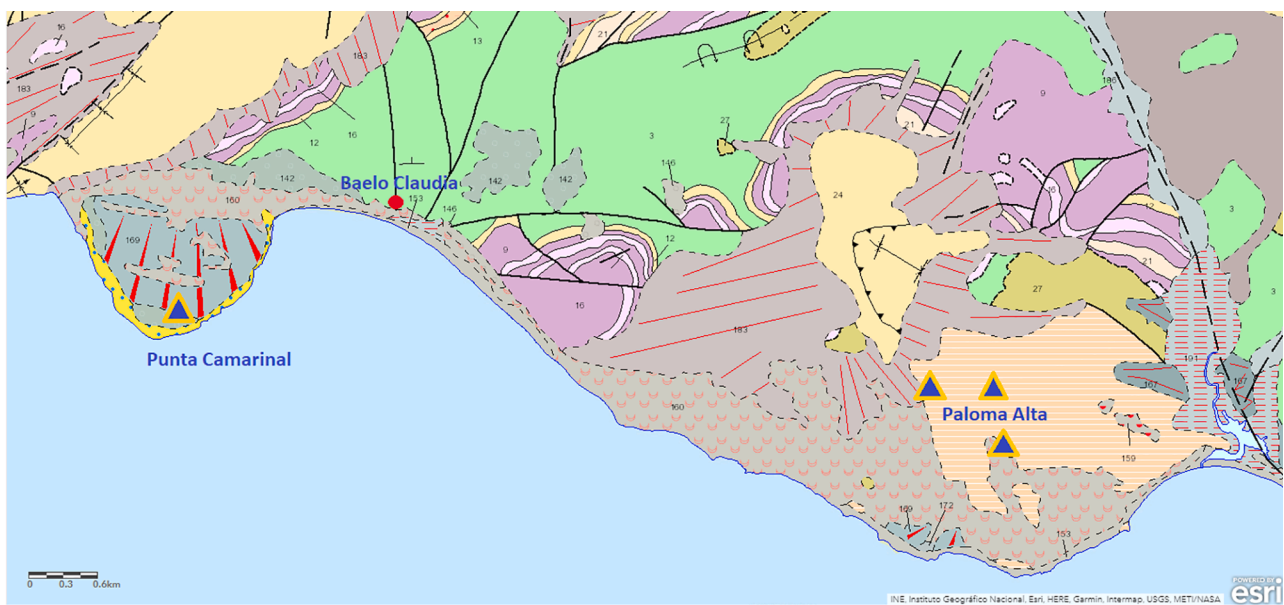
		Chemical composition														
Code	Mineral composition	Mortar					Binder					Aggregates				
		CaO	MgO	SiO ₂	Al ₂ O ₃	Fe ₂ O ₃	CaO	MgO	SiO ₂	Al ₂ O ₃	Fe ₂ O ₃	CaO	MgO	SiO ₂	Al ₂ O ₃	Fe ₂ O ₃
R19	binder: C (main component), G (some samples), A (one sample); aggregate: Ph, Cbz, Sa, CPx, Mca, Ana; +ceramic fragments	CaO+MgO = (70.83-85.03wt.%)		SiO ₂ + Al ₂ O ₃ + Fe ₂ O ₃ = (10.17-26.94wt.%)		
L19	lime-based: Q, C, D, An, K	18.8	1.7	46.4	4.5	4.3	CaO+MgO = (80.89-84.13wt.%)		SiO ₂ + Al ₂ O ₃ + Fe ₂ O ₃ = (12.21-15.21wt.%)							
TB18	lime-based binder: C, Q, Al, An, H, D; aggregate: Q, Al, An, Di, AS	85.15±1.41	1.59±0.1	10.62±1.08	2.63±0.46					
	lime-based binder: C, Q, Al, An, H; aggregate: Q, Al, An, Di, AS	68.70±3.15	3.01±0.71	22.03±1.50	4.87±0.13	7.51±0.42	4.51±0.29	66.35±0.74	13.52±0.18
	lime-based binder: C, Q, Al, An, H; aggregate: Q, Al, An, Di, AS	77.94±1.12	10.11±0.68	7.11±0.76	10.11±0.45	1.55±0.42	2.07±0.29	83.42±2.53	8.13±1.51
OO16	lime mortar: Q, C, Ph	9.6-23.9	1-4.3	40-59	4.6-6.4	1.6-2										
S14	lime-based binder+ pozzolan; aggregate: siliceous; B/A=1/3	41.1	SiO ₂ + Al ₂ O ₃ + Fe ₂ O ₃ = 26.29	
	lime-based binder+ pozzolan; aggregate: siliceous+calcitic; B/A=1/2	32.4	SiO ₂ + Al ₂ O ₃ + Fe ₂ O ₃ = 10.53	
K11	lime-based binder: C, Q, D, F; aggregate: C, Q, D, F, M	38.8	2.03	0.84	0.55	0.49	43	4.33	0.36	1.04	0.36

Vitruvius, in Chapter V, it is explained that the most adequate limestone to be used as raw material is that of high purity and whiteness; in other ways, variable degrees of hydraulicity are obtained. From the thermal analysis and pore structure characterization, it is concluded that variable hydraulicity levels have been actually obtained.

It is important to note that further work is needed to identify potential sources of the raw materials. Focusing on lime, although it is generally assumed that quick lime for mortar was produced close to the source [61], so far no archaeological evidence of kilns has been found in the area. However, the city is located in the Almarchal area (Fig. 22), a limestone geological unit. The feasibility of obtaining quicklime from kilns set at a considerable distance from this archaeological site should also be considered, as there are precedents in other archaeological sites [61]. The strategic location of the city within an active Roman trade route could strengthen this hypothesis. As shown in Fig. 22, there are two abandoned Roman quarry areas near Baelo Claudia, Punta Camarinal, and Paloma Alta. Both areas were used for the extraction and processing of stones (calcareenite and micaceous sandstone, respectively) during the Roman period [66]. It could be hypothesized that the coarser aggregates were obtained from these quarries, but additional geological-mineralogical investigations are required to provide solid evidence. As far as the sand is concerned, the bioclast content suggests that the active sand dunes and/or the sand from Punta Camarinal are the most likely sources of this material.

Finally, since one of the most singular findings is the variation in mortar mix composition, the following hypotheses (including pros and/or cons) could be considered:

- o Different recipes were used for each structural element.
- o That was common practice in long aqueducts. However, neither the dimension of the hydraulic construction nor the typological group composition (as changes are observed in the binder-aggregate ratio within the same unit) fully supports this option.
- o The constructions were built in different stages.
- o A more exact dating would be necessary to corroborate this.
- o Variations in hydraulicity levels could be due to the use of different types of lime and/or the use of different amounts of aggregates.
- o Additional analyses would be required to provide additional data on lime composition (including a comprehensive geological-mineralogical study on material provenance) and aggregates.
- o A nonstandardized and unthorough manufacturing procedure was followed.
- o The evidence of deficient compactation and tooling (i.e. entrapped air pores), as well as the irregular quantity and distribution of brick fragments and pumice-type lithic fragments could reinforce that idea. However, the bond between the structural materials is clearly satisfactory (as shown by the CT images in the interface area).



Code	Geological unit description	Geologic epoch (Age)	material
	Active sand dune	Holocene	sand
	Calcareous sandstone, sand, yellow silt and marl. Littoral	Pleistocene-Miocene (Calabrian-Messinian)	
	Micaceous sandstone and marl	Miocene-Oligocene (Burdigalian-)	sandstone
	Bioclastic limestone and marl	Eocene	clay
	Limestone, marl and clay (Almarchal unit)	Late Cretaceous (Maastrichtian-Turonian)	
	Red clay and marly calcarenite	Oligocene-Eocene	limestone
	Glacis, calcarenite and subangular pebble in clayey-sandy matrix	Pleistocene	
	Roman quarry		

Fig. 22. Roman quarry location, geological unit description, and likely material sources (adapted from “Continuous Geological map of Spain, scale 1/50,000. Cartografía IGME (Instituto Geológico y Minero de España). Madrid, Spain. 2021”).

4. Conclusions

This work has provided valuable insights within an active research field, the microstructural-compositional characterization of historical mortars. Despite the crucial role of Roman mortars in the building history, there is a significant lack of knowledge on their pore system in relation to building techniques and durability factors identification. To overcome this gap, this work provides an assessment using a multidisciplinary methodology linking microstructure, composition, heritage features, and historical legacy. The Roman mortars of the Realillo aqueduct, located at the Archaeological Site of Baelo Claudia, Cádiz (Spain), have been thoroughly analysed, with the aim of gaining the information required to identify durability issues, and enriching the knowledge of the different techniques that were used to manufacture the mortars. This construction is especially interesting from a durability point of view, as in addition to being located in a windy coastal area, the water-proof potential of the material is a major issue.

The samples were characterized by means of complementary experimental techniques: petrography, X-ray computed tomography, X-ray fluorescence, X-ray diffraction (micro and conventional), thermal analysis, pycnometry, physisorption, Hg porosimetry, and SEM-EDS.

The main outcomes of this research related to building techniques and durability are the following.

From the pore structure characterization within a multianalytical approach:

- The pore morphology (CT analysis) has allowed for identifying manufacturing features.
 - o The detected coarse and irregular pores can be attributed to the entrapped air, which can be due to inadequate compactation and tooling.
- The crack pattern (CT analysis) has allowed for identifying building techniques and materials.
 - o As extensive cracking areas are not detected in the matrix, a soft-burned manufacturing procedure can be assumed.
 - o The shrinkage cracking (thin, hairline, and passing through the aggregate) can be due to the use of sea sand as aggregate. The small size of the grains and the large amount of water required during manufacturing contributed to the formation of cracks.
 - o Neither cracks nor detachments are detected in the mortar-unit interface area. The bond between the structural materials is satisfactory, improving the durability.
- The porosity values have provided durability factors.
 - o The open and total porosity values (around 60% and 40%, respectively) can be related to a water-resistant potential worsening.
- The pore morphology (CT) together with the pore size distribution values (physisorption and MIP) have completed the hydraulicity characterization (thermal and X-ray analyses). In addition, durability data have been obtained.
 - o The spherical-shaped porous system (water-released spherical pores), as well as the large number of pores with a diameter less than 1 μm that have been observed, are typical of ancient hydraulic mortars. The C-A-S-H gel (SEM-EDS) indicates the presence of hydraulic phases. The thermal analyses ($\text{CO}_2/\text{H}_2\text{O}$ ratios, SBW values, and CO_2/SBW vs. CO_2 diagram) have evidenced different hydraulic levels (hydraulic or artificial pozzolanic and low hydraulic).
 - o The diameter of the pores (0.77–0.95 μm on average and 10.6 μm maximum) and the porous volume (3.30–12% within the weathering range) also point to the hydraulic nature.
 - o The pore size values contribute to satisfactory binder-aggregate cohesion, enhancing the mechanical performance and minimizing the risk of disintegration.

- o Hydraulicity levels can be directly related to durability potential: weather resistance, wind-driven water ingress barrier, and waterproof properties.

From the compositional characterization within an interdisciplinary approach (including archaeological, geological, and historical data):

- The raw building materials have been characterized:
 - o Quartz-rich seas and (from the Si and bioclast content), lime-based binder (from the high amount of Ca and micritic recarbonated lime detected), pumice-type fragments (isolated and in small quantities), and ceramic fragments (identified visually, from the thermal decomposition of carbonates, and from the C-A-S-H gel).
- The local origin of the raw materials cannot be fully asserted.
 - o No complete archaeological evidence has been found to identify the sources. To date, no kilns have been discovered. The Punta Camarinal and Paloma Alta Roman quarries could have provided the coarser aggregates. The most likely sources of sand are the active sand dunes and the perimeter of Punta Camarinal. More work is needed to identify potential sources and enrich the knowledge about geomaterials from geological-mineralogical data.
- The composition of the mixture is variable.
 - o The differences in composition are highlighted by the binder/aggregate ratios (1/1, 1/2, 1/2.5, and 1/3) and the petrographic classifications (medium to fine-granular, coarse-grained granular, and conglomeratic breccoid). The composition is not stable within the same typological group. The best hydraulic potential has been obtained for the mortar that meets the Vitruvian prescription (sample 05 from the settling tank). The aggregates could be directly related to the improvement of the hydraulic level (as indicated by the binder/whole mortar thermal analysis comparison).
 - o To elucidate the causes of the mortar mix variations, these hypotheses could be considered: (i) Different recipes were used for each structural element; (ii) the constructions were built in different stages; (iii) different hydraulic limes were used as raw materials and/or different admixture amounts were used to enhance hydraulicity; (iv) a non-standardized and unthorough manufacturing procedure was followed.

The results have demonstrated the need to characterize the pore structure of ancient mortars within an interdisciplinary and multi-analytical study. The results and data obtained from different fields (archaeology, architecture, geology, and materials science) have been interrelated. As one of the main novelties of this work, significant information regarding materials, durability, and manufacturing techniques has been obtained from a combined analysis of Computed Tomography together with the microstructure investigation from the micropore to macropore range. Since upgrading/degrading durability factors have been identified, a well-founded preventive remedial conservation campaign could be designed by selecting compatible repair materials for future retrofitting-strengthening-refurbishment works. In addition, the knowledge of historical building techniques and materials has been enriched. This knowledge could guide the design of novel, durable, and efficient structural materials.

CRedit authorship contribution statement

Paloma Pineda: Conceptualization, Methodology, Validation, Formal analysis, Investigation, Resources, Data curation, Writing – original draft, Writing – review & editing, Visualization, Supervision, Project administration, Funding acquisition. **Santiago Medina-Carrasco:** Methodology, Software, Validation, Formal analysis, Investigation, Data curation, Writing – original draft, Visualization. **Alfredo Iranzo:** Data curation, Writing – original draft, Visualization. **Laetitia Borau:**

Resources, Writing – original draft, Visualization. **Iván García-Jiménez**: Resources, Writing – original draft, Supervision, Project administration.

Declaration of Competing Interest

The authors declare that they have no known competing financial interests or personal relationships that could have appeared to influence the work reported in this paper.

Acknowledgements

The experimental campaign has been funded by the “VI Plan Propio de Investigación y Transferencia de la Universidad de Sevilla”.

The analysed materials are part of structures recently excavated within the General Research Project directed by Laetitia Borau (CNRS, France): Water management and construction techniques in the territory of Baelo Claudia during the Antiquity.

The in-situ data collection is part of an ongoing activity authorized and approved by the authorities in charge (Delegación Territorial de Fomento, Infraestructuras, Ordenación del Territorio, Cultura y Patrimonio Histórico de Cádiz, Junta de Andalucía) on preventive conservation of structural materials.

The authors kindly acknowledge the support provided by the personnel of the “Servicios Generales de Investigación-Universidad de Sevilla”.

References

- [1] A. Moropoulou, A.S. Cakmak, G. Biscontin, A. Bakolas, E. Zendri, *Advanced Byzantine cement based composites resisting earthquake stresses: the crushed brick/lime mortars of Justinian's Hagia Sophia*, *Constr. Build. Mater.* 16 (8) (2002) 543–552.
- [2] A. Moropoulou et al., “The role of restoration mortars in the earthquake protection of the kaisariani monastery,” in *ECCOMAS Congress 2016 - Proceedings of the 7th European Congress on Computational Methods in Applied Sciences and Engineering*, 2016, vol. 3, pp. 5340–5358, doi: 10.7712/100016.2184.11793.
- [3] J.M. Maragh, J.C. Weaver, A. Masic, V.P. Shastri, *Large-scale micron-order 3D surface correlative chemical imaging of ancient Roman concrete*, *PLoS ONE* 14 (2) (2019).
- [4] A. Moropoulou, A. Bakolas, K. Bisbikou, *Investigation of the technology of historic mortars*, *J. Cult. Heritage* 1 (1) (2000) 45–58.
- [5] M. Stefanidou, V. Pachtá, S. Konopissi, F. Karkadelidou, I. Papayianni, *Analysis and characterization of hydraulic mortars from ancient cisterns and baths in Greece*, *Mater. Struct. Constr.* 47 (4) (2014) 571–580, <https://doi.org/10.1617/s11527-013-0080-y>.
- [6] P. Pineda, “Ancient Materials and Singular Constructions: Numerical, Experimental, and Heritage Strategies to Preserve Masonry Structures in Seismic Areas,” in *Handbook of Research on Seismic Assessment and Rehabilitation of Historic Structures*, 2015, pp. 629–648.
- [7] P. Pineda, “Ancient Materials and Singular Constructions: Numerical, Experimental and Heritage Strategies to Preserve Masonry Structures in Seismic Areas,” in *Civil and Environmental Engineering: Concepts, Methodologies, Tools, and Applications*, Hershey, PA: IGI Global, 2016, pp. 340–359.
- [8] A. Bakolas, G. Biscontin, A. Moropoulou, E. Zendri, *Characterization of structural byzantine mortars by thermogravimetric analysis*, *Thermochim. Acta* 321 (1–2) (1998) 151–160, [https://doi.org/10.1016/S0040-6031\(98\)00454-7](https://doi.org/10.1016/S0040-6031(98)00454-7).
- [9] C. Rispoli, A. De Bonis, R. Esposito, S.F. Graziano, A. Langella, M. Mercurio, V. Morra, P. Cappelletti, *Unveiling the secrets of Roman craftsmanship: mortars from Piscina Mirabilis (Campi Flegrei, Italy)*, *Archaeol Anthropol Sci* 12 (1) (2020), <https://doi.org/10.1007/s12520-019-00964-8>.
- [10] C. Rispoli, *Ancient roman mortars: mix design, mineralogical composition and minerogenetic secondary processes*, *PLINIUS* 43 (2017) 93–100, <https://doi.org/10.19276/plinius.2017.01013>.
- [11] E. Ontiveros-Ortega, O. Rodríguez-Gutiérrez, A.D. Navarro, *Mineralogical and physical-chemical characterisation of Roman mortars used for monumental substructures on the Hill of San Antonio, in the Roman city of Italica (prov. Baetica, Santiponce, Seville, Spain)*, *J. Archaeol. Sci. Reports* 7 (Jun. 2016) 205–223, <https://doi.org/10.1016/j.jasrep.2016.03.043>.
- [12] J. Schafer, H.K. Hilsdorf, “Ancient and new lime mortars—the correlation between their composition, structure and properties,” in *Conservation of stone and other materials: proceedings of the International RILEM/UNESCO Congress “Conservation of Stone and Other Materials: Research-Industry-Media” held at UNESCO headquarters, Paris, June 29–July 1, 1993, 1993*.
- [13] M. Thomson, J.-E. Lindqvist, J. Elsen, and C. Groot, “Porosity of historic mortars,” *13th Int. Brick Block Mason. Conf.*, no. JULY, 2004.
- [14] M.D. Jackson, et al., *Cement microstructures and durability in Ancient Roman seawater concretes*, *RILEM Bookseries* 7 (2013) 50–76, https://doi.org/10.1007/978-94-007-4635-0_5.
- [15] C. Rispoli, A. De Bonis, V. Guarino, S.F. Graziano, C. Di Benedetto, R. Esposito, V. Morra, P. Cappelletti, *The ancient pozzolanic mortars of the Thermal complex of Baia (Campi Flegrei, Italy)*, *J. Cult. Herit.* 40 (2019) 143–154, <https://doi.org/10.1016/j.culher.2019.05.010>.
- [16] S. Pavía, S. Caro, *An investigation of Roman mortar technology through the petrographic analysis of archaeological material*, *Constr. Build. Mater.* 22 (8) (Aug. 2008) 1807–1811, <https://doi.org/10.1016/j.conbuildmat.2007.05.003>.
- [17] C. Rispoli, S.F. Graziano, C. Di Benedetto, A. De Bonis, V. Guarino, R. Esposito, V. Morra, P. Cappelletti, *New insights of historical mortars beyond pompeii: The example of Villa del Pezzolom, Sorrento Peninsula*, *Minerals* 9 (10) (2019) 575, <https://doi.org/10.3390/min9100575>.
- [18] D. Ergenç, R. Fort, *Multi-technical characterization of Roman mortars from Complutum, Spain*, *Meas. J. Int. Meas. Confed* 147 (2019), <https://doi.org/10.1016/j.measurement.2019.106876>.
- [19] M.S. Shackley, *X-Ray fluorescence spectrometry (XRF) in geoarchaeology*. Springer US, 2011.
- [20] A.M.S. Loureiro, S.P.A. Paz, M.d.R. Veiga, R.S. Angélica, *Assessment of compatibility between historic mortars and lime-METAKAOLIN restoration mortars made from amazon industrial waste*, *Appl. Clay Sci.* 198 (2020) 105843, <https://doi.org/10.1016/j.clay.2020.105843>.
- [21] P. Maravelaki-Kalaitzaki, A. Bakolas, I. Karatasios, V. Kilikoglou, *Hydraulic lime mortars for the restoration of historic masonry in Crete*, *Cem. Concr. Res.* 35 (8) (2005) 1577–1586, <https://doi.org/10.1016/j.cemconres.2004.09.001>.
- [22] M. Schreiner, B. Frühmann, D. Jembrih-Simbürger, R. Linke, *X-rays in art and archaeology: an overview*, *Powder Diffr.* 19 (1) (2004) 3–11, <https://doi.org/10.1154/1.1649963>.
- [23] A. Duran, J.L. Perez-Rodriguez, M.C.J. De Haro, *Study of the gilding technique used in polychromed stones and ceramics by dedicated laboratory-made micro X-ray diffraction and complementary techniques*, *Anal. Bioanal. Chem.* 394 (6) (2009) 1671–1677, <https://doi.org/10.1007/s00216-009-2836-3>.
- [24] M.L. Franquelo, A. Duran, J. Castaing, D. Arquillo, J.L. Perez-Rodriguez, *XRF, μ -XRD and μ -spectroscopic techniques for revealing the composition and structure of paint layers on polychrome sculptures after multiple restorations*, *Talanta* 89 (2012) 462–469, <https://doi.org/10.1016/j.talanta.2011.12.063>.
- [25] U. P. and K. L. S. Bob B. He, “Comparison between conventional and two - dimensional XRD,” *Denver X-ray Conf. Appl. X-ray Anal.*, vol. 16, no. 1, pp. 1–7, 2009, doi: 10.4028/www.scientific.net/MSF.278-281.151.
- [26] B.B. He, U. Preckwinkel, K.L. Smith, *Fundamentals of two-dimensional X-ray diffraction (XRD2)*, *Adv. X-ray Anal.* 43 (1999) 273–280, <https://doi.org/10.1154/1.1577355>.
- [27] P. Maravelaki-Kalaitzaki, A. Bakolas, A. Moropoulou, *Physico-chemical study of Cretan ancient mortars*, *Cem. Concr. Res.* 33 (5) (May 2003) 651–661, [https://doi.org/10.1016/S0008-8846\(02\)01030-X](https://doi.org/10.1016/S0008-8846(02)01030-X).
- [28] A. Moropoulou, A. Bakolas, K. Bisbikou, *Physico-chemical adhesion and cohesion bonds in joint mortars imparting durability to the historic structures*, *Constr. Build. Mater.* 14 (1) (Feb. 2000) 35–46, [https://doi.org/10.1016/S0950-0618\(99\)00045-8](https://doi.org/10.1016/S0950-0618(99)00045-8).
- [29] C. Genestar, C. Pons, A. Más, *Analytical characterisation of ancient mortars from the archaeological Roman city of Pollentia (Balearic Islands, Spain)*, *Anal. Chim. Acta* 557 (1–2) (Jan. 2006) 373–379, <https://doi.org/10.1016/j.aca.2005.10.058>.
- [30] S. Divya Rani, A.V. Rahul, M. Santhanam, *A multi-analytical approach for pore structure assessment in historic lime mortars*, *Constr. Build. Mater.* 272 (2021) 121905, <https://doi.org/10.1016/j.conbuildmat.2020.121905>.
- [31] L. Borau, *Water management and steep gradient: the example of the roman city of Baelo Claudia (Spain)*, in *Tamburrino E., Zanollo P. Aquam Ducere, 3. Water management in arid and semiarid climates in Roman time, Materiali della 3a International Summer School, Feltre, Seren del Grappa, D. Edizioni (2019) 17–26*.
- [32] L. Borau, *Difusión de modelos técnicos romanos: particularidades del sistema de abastecimiento de agua a la ciudad de Baelo Claudia*, *Arch. Español Arqueol* 88 (2015) 149–169.
- [33] L. Borau, *L'eau dans la fabrique de la ville : état de la recherche à Baelo Claudia*, *Melanges Casa Velazquez* 1 (2017) 97–120.
- [34] P. Sillières, “Baelo Claudia. Una Ciudad romana de la Bética,” 2005.
- [35] P. Pineda, A. Iranzo, *Analysis of sand-loaded air flow erosion in heritage sites by Computational Fluid Dynamics: Method and damage prediction*, *J. Cult. Herit.* 25 (Jan. 2017) 75–86, <https://doi.org/10.1016/j.culher.2016.12.005>.
- [36] L. Binda, A. Saisi, C. Tiraboschi, *Investigation procedures for the diagnosis of historic masonries*, *Constr. Build. Mater.* 14 (4) (Jun. 2000) 199–233, [https://doi.org/10.1016/S0950-0618\(00\)00018-0](https://doi.org/10.1016/S0950-0618(00)00018-0).
- [37] B. Middendorf, J. J. Hughes, K. Callebaut, G. Baronio, and I. Papayianni, “Investigative methods for the characterisation of historic mortars - Part 1: Mineralogical characterisation,” *Mater. Struct. Constr.*, vol. 38, no. 282, 2005, doi: 10.1617/14281.
- [38] B. Middendorf, G. Baronio, K. Callebaut, J. J. Hughes, P. Bartos, and C. Groot, “Chemical-mineralogical and physical-mechanical investigations of old mortars,” in *International RILEM Workshop on Historic Mortars: Characteristics and Tests: Paisley, Scotland, 12th–14th May 1999, 2000*.
- [39] B. Middendorf, J. J. Hughes, K. Callebaut, G. Baronio, and I. Papayianni, “Investigative methods for the characterisation of historic mortars - Part 2: Chemical characterisation,” *Mater. Struct. Constr.*, vol. 38, no. 282, 2005, doi: 10.1617/14282.
- [40] C.R. Hubbard, R.L. Snyder, *RIR — measurement and use in quantitative XRD*, *Powder Diffr.* 3 (2) (1988) 74–77, <https://doi.org/10.1017/S0885715600013257>.

- [41] R.L. Snyder, The use of reference intensity ratios in X-ray quantitative analysis, *Powder Diffr.* 7 (4) (1992) 186–193, <https://doi.org/10.1017/S0885715600018686>.
- [42] Bruker AXS, "TOPAS V6: General profile and structure analysis software for powder diffraction data. - Users manual, Bruker AXS, Karlsruhe, Germany." 2017.
- [43] H.M. Rietveld, A profile refinement method for nuclear and magnetic structures, *J. Appl. Crystallogr.* 2 (2) (1969) 65–71, <https://doi.org/10.1107/S0021889869006558>.
- [44] R. A. Young, "The Rietveld Method," by RA Young. *Oxford University Press, Oxford.* p. 312, 1993, doi: 10.1017/CBO9781107415324.004.
- [45] G.M. Ingo, I. Fragalà, G. Bultrini, T. de Caro, C. Riccucci, G. Chiozzini, Thermal and microchemical investigation of Phoenician-Punic mortars used for lining cisterns at Tharros (western Sardinia, Italy), *Thermochim Acta* 418 (1-2) (2004) 53–60, <https://doi.org/10.1016/j.tca.2003.11.053>.
- [46] F. Gonzalez García, G. García Ramos, Arcillas cerámicas de Andalucía I. Yacimientos de las vegas del Guadalquivir y Corbones en la provincia de Sevilla, *Boletín la Soc. Española Cerámica y Vidr.* 3 (5) (1964) 481–502.
- [47] A. Bernal Dueñas, G. García Ramos, F. Gonzalez García, A. Justo Erbez, J.L. Perez-Rodríguez, Arcillas cerámicas de Andalucía 11. Yacimientos terciarios y cuaternarios de la margen derecha del Guadalquivir en la provincia de Jaén, *Boletín la Soc. Española Cerámica y Vidr.* 16 (6) (1977) 353–360.
- [48] S. Suwas, R. K. Ray, R. K. R. Satyam Suwas, Crystallographic Texture of Materials. 2014.
- [49] A. Bakolas, G. Biscontin, V. Contardi, E. Franceschi, A. Moropoulou, D. Palazzi, E. Zendri, Thermoanalytical research on traditional mortars in Venice, *Thermochim. Acta* 269-270 (1995) 817–828, [https://doi.org/10.1016/0040-6031\(95\)02574-X](https://doi.org/10.1016/0040-6031(95)02574-X).
- [50] H. Böke, S. Akkurt, B. Ipekoğlu, E. Uğurlu, Characteristics of brick used as aggregate in historic brick-lime mortars and plasters, *Cem. Concr. Res.* 36 (6) (Jun. 2006) 1115–1122, <https://doi.org/10.1016/j.cemconres.2006.03.011>.
- [51] D. Ergenç, R.F. González, Preliminary investigation of the preparation of repair mortars for the Temple Of Diana, Mérida, Spain, *Ge-Conservacion* 1 (11) (2017) 42–49, <https://doi.org/10.37558/gec.v1i11.443>.
- [52] G.M. Ingo, I. Fragalà, G. Bultrini, T. De Caro, C. Riccucci, G. Chiozzini, Thermal and microchemical investigation of Phoenician-Punic mortars used for lining cisterns at Tharros (western Sardinia, Italy), *Thermochim Acta* 418 (1–2) (Aug. 2004) 53–60, <https://doi.org/10.1016/j.tca.2003.11.053>.
- [53] A. Bonazza, et al., Characterization of hydraulic mortars from archaeological complexes in Petra, *Period. di Mineral.* 82 (3) (2013) 459–475, <https://doi.org/10.2451/2013PM0027>.
- [54] M. Drdácý, F. Fratini, D. Frankeová, Z. Slížková, The Roman mortars used in the construction of the Ponte di Augusto (Narni, Italy) – a comprehensive assessment, *Constr. Build. Mater.* 38 (2013) 1117–1128, <https://doi.org/10.1016/j.conbuildmat.2012.09.044>.
- [55] H. J. P. Brocken, O. C. G. Adant, and L. Pel, "Moisture transport properties of mortar and mortar joint: A NMR study," *Heron*, vol. 42, no. 1, 1997.
- [56] M. Franzini, L. Leoni, M. Lezzerini, A procedure for determining the chemical composition of binder and aggregate in ancient mortars: its application to mortars from some medieval buildings in Pisa, *J. Cult. Heritage* 1 (4) (2000) 365–373.
- [57] S. Kramar, V. Zalar, M. Urosevic, W. Körner, A. Mauko, B. Mirtič, J. Lux, A. Mladenović, Mineralogical and microstructural studies of mortars from the bath complex of the Roman villa rustica near Mošnje (Slovenia), *Mater. Charact.* 62 (11) (2011) 1042–1057, <https://doi.org/10.1016/j.matchar.2011.07.019>.
- [58] Iupac, Manual of symbols and terminology, Appendix 2, Pt. 1, colloid and surface chemistry, *Pure Appl. Chem.* 31 (1972) 578.
- [59] J. Lanás, J.L.P. Bernal, M.A. Bello, J.I.A. Galindo, Mechanical properties of natural hydraulic lime-based mortars, *Cem. Concr. Res.* 34 (12) (2004) 2191–2201, <https://doi.org/10.1016/j.cemconres.2004.02.005>.
- [60] A. Farci, D. Floris, P. Meloni, Water permeability vs. porosity in samples of Roman mortars, *J. Cult. Herit.* 6 (1) (2005) 55–59, <https://doi.org/10.1016/j.culher.2004.08.002>.
- [61] E.A. Laycock, D. Pirrie, F. Clegg, A.M.T. Bell, P. Bidwell, An investigation to establish the source of the Roman lime mortars used in Wallsend, UK, *Constr. Build. Mater.* 196 (2019) 611–625, <https://doi.org/10.1016/j.conbuildmat.2018.11.108>.
- [62] B. Taşlı and H. Böke, "Properties of Roman lime mortars in ancient Lycia region," in *AIP Conference Proceedings*, 2018, vol. 2022, doi: 10.1063/1.5060692.
- [63] I. Polat-Pekmezci and A. Ersen, "Characterization of Roman Mortars and Plasters in Tarsus (Cilicia-Turkey)," in 2nd Historic Mortars Conference HMC2010 and RILEM TC 203-RHM Final Workshop, Sep. 2010, pp. 317–324.
- [64] A. Moropoulou, A. Bakolas, S. Anagnostopoulou, Composite materials in ancient structures, *Cem. Concr. Compos.* 27 (2) (2005) 295–300.
- [65] Vitruvius, *The Ten Books of Architecture*. 1914.
- [66] S. Domínguez-Bella, "Materiales rocosos en la construcción de Baelo Claudia. Análisis arqueométrico y geoarqueología de las canteras de Paloma Alta y Punta Camarinal," in II Jornadas Internacionales de Baelo Claudia: Nuevas Investigaciones, 2010, pp. 93–106.